

The Evolution of the He II-Ionizing Background at Redshifts $2.3 < z < 3.8$ Inferred from a Statistical Sample of 24 *HST*/COS He II Ly α Absorption Spectra *

GÁBOR WORSECK,^{1,2} FREDERICK B. DAVIES,^{1,3} JOSEPH F. HENNAWI,^{1,3} AND J. XAVIER PROCHASKA^{4,5}

¹Max-Planck-Institut für Astronomie, Königstuhl 17, D-69117 Heidelberg, Germany

²Institut für Physik und Astronomie, Universität Potsdam, Karl-Liebknecht-Str. 24/25, D-14476 Potsdam, Germany

³Department of Physics, University of California, Santa Barbara, CA 93106, USA

⁴Department of Astronomy and Astrophysics, University of California, 1156 High Street, Santa Cruz, CA 95064, USA

⁵University of California Observatories, Lick Observatory, 1156 High Street, Santa Cruz, CA 95064, USA

(Received 2018 August 15; Revised 2019 February 28; Accepted 2019 March 5)

ABSTRACT

We present measurements of the large-scale (≈ 40 comoving Mpc) effective optical depth of He II Ly α absorption, τ_{eff} , at $2.54 < z < 3.86$ toward 16 He II-transparent quasars observed with the Cosmic Origins Spectrograph (COS) on the *Hubble Space Telescope* (*HST*), to characterize the ionization state of helium in the intergalactic medium (IGM). We provide the first statistical sample of τ_{eff} measurements in six signal-to-noise ratio $\gtrsim 3$ He II sightlines at $z > 3.5$, and study the redshift evolution and sightline-to-sightline variance of τ_{eff} in 24 He II sightlines. We confirm an increase of the median τ_{eff} from ≈ 2 at $z = 2.7$ to $\tau_{\text{eff}} \gtrsim 5$ at $z > 3$, and a scatter in τ_{eff} that increases with redshift. The $z > 3.5$ He II absorption is predominantly saturated, but isolated narrow ($\Delta v < 650 \text{ km s}^{-1}$) transmission spikes indicate patches of reionized helium. We compare our measurements to predictions for a range of UV background models applied to outputs of a large-volume (146 comoving Mpc)³ hydrodynamical simulation by forward-modeling our sample's quality and size. At $z > 2.74$ the variance in τ_{eff} significantly exceeds expectations for a spatially uniform UV background, but is consistent with a fluctuating radiation field sourced by variations in the quasar number density and the mean free path in the post-reionization IGM. We develop a method to infer the approximate median He II photoionization rate Γ_{HeII} of a fluctuating UV background from the median τ_{eff} , finding a factor ≈ 5 decrease in Γ_{HeII} between $z \approx 2.6$ and $z \approx 3.1$. At $z \approx 3.1$ a $\Gamma_{\text{HeII}} = [9.1_{-1.2}^{+1.1} \text{ (stat.) }_{-3.4}^{+2.4} \text{ (sys.)}] \times 10^{-16} \text{ s}^{-1}$ corresponds to a median He II fraction of $\approx 2.5\%$, indicating that our data probe the tail end of He II reionization.

Keywords: dark ages, reionization, first stars – diffuse radiation – intergalactic medium – quasars: absorption lines

1. INTRODUCTION

The epoch of helium reionization marked the final baryonic phase transition to substantially influence the thermal and ionization state of the IGM. While hydrogen reionization occurred at $z \gtrsim 6$ (e.g., Fan et al. 2006; Becker et al. 2015; Davies et al. 2018b; Planck Collaboration et al. 2018), the completion of He II reionization was likely delayed to $z \sim 3$ when quasars became numerous enough to supply

the required hard ($E = h\nu > 54.4 \text{ eV}$) UV photons (e.g. Madau & Meiksin 1994; Miralda-Escudé et al. 2000; McQuinn et al. 2009; Compostella et al. 2013, 2014). The current picture of a quasar-driven He II reionization process extending over ~ 1 Gyr is supported by most measurements of the $z > 3$ quasar luminosity function (e.g., Hopkins et al. 2007; McGreer et al. 2013; Jiang et al. 2016; Kulkarni et al. 2018b), which yield a total quasar emissivity sufficient to complete He II reionization by $z \sim 3$ (Madau et al. 1999; Miralda-Escudé et al. 2000; Wyithe & Loeb 2003; Furlanetto & Oh 2008a; Haardt & Madau 2012; La Plante & Trac 2016; Khaire 2017; Puchwein et al. 2019; Kulkarni et al. 2018b). However, such photon budget arguments only provide rough constraints on the He II reionization history due to their simplified treatment of the gas density distribution, in particular the gradual reionization of optically thick absorbers near the end of reionization (Bolton et al. 2009a; Madau 2017).

Corresponding author: Gábor Worseck
gworseck@uni-potsdam.de

* Based on observations made with the NASA/ESA *Hubble Space Telescope*, obtained at the Space Telescope Science Institute, which is operated by the Association of Universities for Research in Astronomy, Inc., under NASA contract NAS5-26555. These observations are associated with Programs 13013 and 13875. Archival *Hubble Space Telescope* data (Programs 7575, 9350, 11528, 12033, 12178, 12249, 12816) were obtained from the Mikulski Archive for Space Telescopes (MAST).

Semianalytic models and detailed cosmological radiative transfer simulations that self-consistently include the physics governing He II reionization both predict that the bulk of intergalactic He II was reionized by the emerging quasar population at $z \lesssim 5$, and ended with the percolation of the He III zones around quasars at $z \sim 3$ (Fardal et al. 1998; Miralda-Escudé et al. 2000; Sokasian et al. 2002; Gleser et al. 2005; Furlanetto & Oh 2008a; Tittley & Meiksin 2007; Furlanetto 2009; Faucher-Giguère et al. 2009; McQuinn et al. 2009; Furlanetto & Dixon 2010; Meiksin & Tittley 2012; Compostella et al. 2013, 2014). However, there remains significant uncertainty in the precise timing and morphology of He II reionization, as the detailed conditions of the intergalactic gas during and after He II reionization depend on several poorly constrained parameters of the high-redshift quasar population (e.g. their duty cycle, spectral energy distribution and opening angle), and the frequency and structure of self-shielding absorbers. Typically, several generations of quasars are required to fully reionize a given region, resulting in a rich thermal and ionization structure of the gas (Compostella et al. 2013, 2014).

Over the last two decades much theoretical and observational work has focused on the thermal state of the IGM during and after He II reionization. During He II reionization supersonic quasar ionization fronts impulsively heat the IGM which subsequently relaxes to a tight post-reionization power-law temperature-density relation governed by adiabatic (Hubble) cooling and photoheating by a quasi-homogeneous UV background (e.g. Hui & Gnedin 1997; Haehnelt & Steinmetz 1998; Furlanetto & Oh 2008b; Bolton et al. 2009b; McQuinn 2009; Becker et al. 2011; Compostella et al. 2013, 2014; Puchwein et al. 2015; McQuinn & Upton Sanderbeck 2016; La Plante et al. 2017). The exact amount of injected heat ($\Delta T = 5,000\text{--}10,000$ K) depends on the duration of He II reionization, the spatial clustering of the sources, and their typical spectral energy distribution (Tittley & Meiksin 2007; Bolton et al. 2009a; McQuinn 2009; Compostella et al. 2013, 2014; Puchwein et al. 2015). Information on the thermal state of the IGM has been extracted from the H I Ly α forest by decomposing it into individual absorption lines (Schaye et al. 2000; Ricotti et al. 2000; Bryan & Machacek 2000; McDonald et al. 2001; Rudie et al. 2012; Bolton et al. 2014; Rorai et al. 2018; Hiss et al. 2018) or by treating it as a continuous field using various transmission statistics, i.e. the probability distribution function (Bolton et al. 2008; Viel et al. 2009; Calura et al. 2012; Lee et al. 2015; Rorai et al. 2017a), the power spectrum (Zaldarriaga et al. 2001; Walther et al. 2018, 2019), the transmission curvature (Becker et al. 2011; Boera et al. 2014), wavelet decomposition (Theuns et al. 2002; Theuns et al. 2002; Lidz et al. 2010; Garzilli et al. 2012), and the quasar pair phase angle distribution (Rorai et al. 2017b). Despite large statistical errors and some remaining tension between the measurements, these studies indicate an extended heating of the IGM from $z \approx 6$ (Bolton et al. 2010; Bolton et al. 2012) to $z \approx 2.8$ (Schaye et al. 2000; Becker et al. 2011; Boera et al. 2014; Hiss et al. 2018) expected

from an extended He II reionization process. Very recent results from Walther et al. (2019) show a rise in the IGM temperature from $z = 5$, peaking at $z \sim 3.4$, and subsequent cooling to $z = 1.8$, which can only be explained as being a result of extended He II reionization. The He II reionization epoch can be studied directly via spectroscopy of intergalactic He II Ly α absorption ($\lambda_{\text{rest}} = 303.78$ Å) toward far-UV (FUV)-bright quasars at $z > 2$. The discovery and systematic study of the He II Ly α forest at $z \gtrsim 2.7$ has been a science driver for *HST* since its inception (Bahcall 1979). However, despite extensive efforts during the first 15 years of *HST* operations, only seven He II sightlines had been successfully probed, because for most $z_{\text{em}} > 2.7$ quasars the spectral range covering the He II Lyman series is blacked out by optically thick H I Lyman limit systems in the foreground IGM (Picard & Jakobsen 1993; Worseck & Prochaska 2011). Early *HST* spectra of varying spectral resolution and quality revealed strong evolution of the He II Ly α effective optical depth τ_{eff} from Gunn-Peterson troughs ($\tau_{\text{eff}} \gtrsim 3$) measured toward four $z_{\text{em}} > 3$ quasars (Jakobsen et al. 1994; Hogan et al. 1997; Anderson et al. 1999; Heap et al. 2000; Zheng et al. 2004a, 2008) to fluctuating He II absorption at $2.7 \lesssim z \lesssim 2.9$ (Reimers et al. 1997, 2005; Heap et al. 2000; Smette et al. 2002). High-resolution spectra taken with the *Far Ultraviolet Spectroscopic Explorer* (*FUSE*, $R = \lambda/\Delta\lambda \approx 20,000$) resolved the He II Ly α forest in two sightlines (Kriss et al. 2001; Shull et al. 2004; Zheng et al. 2004b; Fechner et al. 2006; Fechner & Reimers 2007). Inferences on the He II reionization history, however, were severely limited by sample variance and data quality (McQuinn et al. 2009; Furlanetto & Dixon 2010).

The first panoramic FUV imaging surveys by the *Galaxy Evolution Explorer* (*GALEX*, Martin et al. 2005; Morrissey et al. 2007) enabled the efficient photometric selection of likely He II-transparent quasar sightlines (Syphers et al. 2009a,b; Worseck & Prochaska 2011). *HST* follow-up spectroscopy with the FUV-sensitive Cosmic Origins Spectrograph (COS, Green et al. 2012) yielded a sample of 11 new science-grade (signal-to-noise ratio $S/N \gtrsim 3$) He II Ly α absorption spectra covering $2.7 \lesssim z \lesssim 3.8$ (Worseck et al. 2011; Syphers et al. 2012; Zheng et al. 2015; Worseck et al. 2016). Together with high-quality COS spectra of the previously known sightlines (Shull et al. 2010; Syphers & Shull 2013; Syphers & Shull 2014), these new sightlines enabled statistical studies of the intergalactic He II Ly α opacity and constraints on the He II reionization history. The diminishing sightline-to-sightline variance in the large-scale (~ 40 comoving Mpc) He II effective optical depth indicates that He II reionization completed at $z \approx 2.7$ (Worseck et al. 2011).

In Worseck et al. (2016, hereafter W16) we presented first results of the Helium Reionization Survey (HERS), a comprehensive campaign to study the epoch of He II reionization with *HST* He II absorption spectra. Our analysis of 17 sightlines revealed a gradual increase in the He II effective optical depth from $z = 2.3$ ($\tau_{\text{eff}} \approx 1$) to $z = 3.4$ ($\tau_{\text{eff}} \gtrsim 4.5$) with strong sightline-to-sightline variance at $z > 2.7$, con-

sistent with a predominantly ionized IGM with large UV background fluctuations (Davies & Furlanetto 2014; Davies et al. 2017, hereafter D17). Numerical simulations of quasar-driven He II reionization struggle to reproduce the observed distribution of He II effective optical depths at $z \approx 3.4$ (McQuinn et al. 2009; Compostella et al. 2013), suggesting a very extended epoch of He II reionization (W16). However, this apparent tension may be due to the limited number of quasar models run in limited simulation volumes (D’Aloisio et al. 2017), or due to the small number of four He II sightlines covering $z \approx 3.4$ (Compostella et al. 2014). A large population of faint quasars may accomplish He II reionization at $z > 4$ (Madau & Haardt 2015), but underpredicts the observed He II effective optical depths at $2.7 < z < 3$ (Worseck et al. 2016; Mitra et al. 2018; Puchwein et al. 2019; Garaldi et al. 2019) unless the post-reionization UV background is strongly fluctuating on large scales (Furlanetto & Dixon 2010; McQuinn & Worseck 2014; Davies & Furlanetto 2014; D17). Likewise, an early He II reionization would prematurely heat the IGM (D’Aloisio et al. 2017; Mitra et al. 2018; Puchwein et al. 2019; Garaldi et al. 2019). Similarly, the H I effective optical depths display a large sightline-to-sightline variance at $z > 5.5$ (Becker et al. 2015), possibly persisting to $z \approx 5.2$ (Bosman et al. 2018; Eilers et al. 2018). These may be explained by relic temperature fluctuations from patchy H I reionization (D’Aloisio et al. 2015; Keating et al. 2018) and/or large UV background fluctuations that are either sourced by clustered galaxies and a short mean free path to ionizing photons (Davies & Furlanetto 2016; Davies et al. 2018a; D’Aloisio et al. 2018; Becker et al. 2018) or rare bright sources, such as quasars (Chardin et al. 2015, 2017). While quasars are likely not abundant enough to substantially contribute to the $z \gtrsim 5$ H I-ionizing UV background and H I reionization (e.g. Jiang et al. 2016; Ricci et al. 2017; McGreer et al. 2018; Parsa et al. 2018; Matsuoka et al. 2018; Kulkarni et al. 2018b; Wang et al. 2018, but see Giallongo et al. 2015), it may be necessary to include them in reionization models in order to explain the fluctuations in the effective optical depths of H I at $z > 5.5$ (Chardin et al. 2015, 2017, although see Kulkarni et al. 2018a) and of He II at $z \approx 3.4$ (Compostella et al. 2014).

In light of this heated debate on the duration of He II reionization, the sources of reionization, and the high-redshift UV background, it is timely to extend the sample of He II absorption measurements, particularly at $z > 3$. In this manuscript we present *HST/COS* spectra of eight additional He II-transparent quasars (Section 2) that more than double the redshift pathlength sensitive to $\tau_{\text{eff}} \sim 5$ at $3 < z < 3.5$, and provide a statistically meaningful sample of six He II sightlines probing $z > 3.5$ (Section 3). With an enlarged sample of measured He II effective optical depths (Section 4) and using realistic forward-modeled mock spectra from a large-volume hydrodynamical simulation (Lukić et al. 2015), we test recent models of the He II-ionizing background (D17; Puchwein et al. 2019), and provide measurements of the evolving He II photoionization rate and the corresponding

He II fraction at $2.3 < z < 3.86$ (Sections 5 and 6). We conclude in Section 7.

We adopt a flat cold dark matter cosmology with dimensionless Hubble constant $h = 0.685$ ($H_0 = 100h \text{ km s}^{-1} \text{ Mpc}^{-1}$) and density parameters $(\Omega_{\text{m}}, \Omega_{\text{b}}, \Omega_{\Lambda}) = (0.3, 0.047, 0.7)$ for total matter, baryons, and cosmological constant, consistent with Planck Collaboration et al. (2018). In this cosmology $\Delta z = 0.04$ – the standard interval that we will use for our τ_{eff} measurements – corresponds to a distance interval of ≈ 40 comoving Mpc (hereafter cMpc) at $z = 3$. The object designations of quasars discovered by SDSS will be abbreviated to SDSS JHHMM±DDMM.

2. OBSERVATIONS AND DATA REDUCTION

2.1. Discovery of FUV-Bright $z_{\text{em}} > 3.1$ Quasars

Our sample includes six He II-transparent sightlines toward FUV-bright $z_{\text{em}} > 3.1$ quasars discovered in our dedicated ground-based survey, dubbed the ‘He II Quasar Survey’ (HE2QS, Worseck et al. in preparation), which we will briefly summarize here. Our survey was motivated by the dearth of UV-bright $z_{\text{em}} \gtrsim 3$ quasars that is due to a combination of physical effects (i.e. the declining space density of bright quasars and the incidence of optically thick H I Lyman limit systems in the IGM) and optical color selection effects (Worseck & Prochaska 2011). While matching *GALEX* photometry to existing quasar catalogs had led to many tens of candidates (Syphers et al. 2009a,b; Worseck & Prochaska 2011), only 11 of these were either bright enough for efficient science-grade ($S/N \gtrsim 3$) spectroscopic follow-up with *HST/COS* ($FUV \lesssim 21.5$; Worseck et al. 2011; Syphers et al. 2012; Worseck et al. 2016) or probed $z > 3.5$, justifying exposure times $\gtrsim 20$ ks (Zheng et al. 2015; Worseck et al. 2016).

Target selection was performed mainly via applying color cuts to combined catalogs of wide-field multi-wavelength photometry from *GALEX* (FUV and NUV; Morrissey et al. 2007), SDSS (*ugri*; e.g. Aihara et al. 2011) or Pan-STARRS (*gri*; Chambers et al. 2016), and *WISE* (W1 and W2; Wright et al. 2010). Typically we required significant flux in the FUV ($S/N > 3$, $FUV < 21.5$) and the optical ($i < 19.5$) to ensure efficient spectroscopic follow-up with *HST/COS* and ground-based telescopes, respectively. On the SDSS footprint we also applied extreme deconvolution techniques (Bovy et al. 2011a,b) specifically trained on SDSS+*GALEX* mock photometry (Worseck & Prochaska 2011) to select FUV-bright high- z quasar candidates. The quasar candidates were verified with low-resolution ($R \sim 200$) optical spectroscopy, mainly with the Calar Alto Faint Object Spectrograph (CAFOS) at the Calar Alto 2.2 m telescope and the Kast spectrometer at the Lick 3 m Shane Telescope during several campaigns (2010–2015). Unambiguous redshifts were measured from broad emission lines (typically H I Ly α and C IV).

2.2. *HST/COS* Follow-up Spectroscopy

In *HST* Cycles 20 and 22 we used COS (Green et al. 2012) to obtain follow-up spectroscopy of eight $3.1 < z_{\text{em}} < 3.8$

quasars discovered in HE2QS (Programs 13013 and 13875, PI Worseck; Table 1). The UV brightness of our targets enabled efficient, simultaneous verification of quasar flux at He II Ly α in the quasar rest frame and science-grade spectroscopy of the He II absorption along their sightlines in single visits of 3–4 *HST* orbits per target. We employed the COS grating G140L in the 1105 Å setup ($\lambda\lambda$ 1110–2150 Å) at COS Lifetime Positions (LPs) 2 and 3, resulting in a spectral resolution $R \simeq 1400$ (LP2) and $R \simeq 1600$ (LP3) at 1150 Å. The 20–30% lower spectral resolution compared to COS LP1 is inconsequential to our science goal to quantify the He II absorption on scales $\Delta z \geq 0.01$ ($\gtrsim 4$ G140L resolution elements). The Cycle 20 observations were taken between 2013 April and December, i.e. in a period of high solar activity, while the Cycle 22 observations were taken between 2015 August and November, i.e. past solar maximum. In our Cycle 22 program we also obtained science-grade COS G140L spectra of two $z_{\text{em}} \simeq 3.8$ SDSS quasars that had been verified to show flux at He II Ly α in earlier surveys with STIS (Zheng et al. 2005) and the ACS prism (Syphers et al. 2009a). Being a factor $\gtrsim 2$ fainter than the quasars discovered in HE2QS, these two targets needed significantly longer exposures of 2×5 orbits to yield S/N= 3–4 at He II Ly α . Individual visits were scheduled within two months of another to minimize complications in the coaddition of very low S/N data due to quasar variability.

2.3. Archival Data

We supplemented this data set with *HST* spectra of 17 He II-transparent quasars studied in W16, but using more recent higher-quality COS G130M spectra for four of these (Table 1). Q 0302–003 (Syphers & Shull 2014) was reobserved in the COS GTO Cycle 18 Program 12033 (PI Green) at COS LP1 ($R \simeq 16,000$ at 1150 Å). Three UV-bright He II-transparent quasars discovered in a COS G140L survey by Syphers et al. (2012) were followed up with G130M in its 1222 Å setup between 2013 March and July (Cycle 20 Program 12816, PI Syphers). Compared to the redder G130M setups, the 1222 Å setup ($\lambda\lambda$ 1066–1367 Å) provides extended coverage of the He II Ly α absorption down to $z = 2.51$ at lower spectral resolution ($R \simeq 15,000$ at 1150 Å, declining toward shorter and longer wavelengths). Visits were scheduled within a few days of each other to minimize the adverse effects of quasar variability. For the highest-redshift target HS 0911+4809 at $z_{\text{em}} = 3.350$ a 1-orbit G140L spectrum was taken together with the G130M spectrum to aid continuum definition and to gauge the level of quasar variability between the G140L survey observations in Cycle 18 and the G130M follow-up in Cycle 20.

2.4. *HST*/COS Data Reduction

All raw data were retrieved from the *HST* archive and were reduced with the CALCOS pipeline (v2.21) and custom software that preserves Poisson counts in coadded spectra and offers reliable background subtraction (dark current, quasi-diffuse sky emission and scattered light) at the flux limit of *HST*/COS ($f_{\lambda} \lesssim 10^{-17}$ erg cm $^{-2}$ s $^{-1}$ Å $^{-1}$; W16). The only

significant update to the procedure detailed in W16 is that we routinely limited the COS detector pulse height amplitude (PHA) to the range encountered in the science data, which effectively excludes a part of the background and therefore maximizes the sensitivity to high τ_{eff} at $z > 3.3$ where the COS G140L sensitivity significantly declines (W16). Pulse height screening was employed for all G130M spectra and for G140L spectra obtained in Programs 12249, 13013 and 13875. With the reanalyzed data from Program 12249 we confirmed that for G140L He II spectra, pulse height screening significantly enhances the data quality only at $z > 3.3$, so we took 8 lower-redshift sightlines from W16 without reprocessing them (Table 1).

The data reduction parameters were customized according to the LP, the grating setting, and the changing PHA distribution of the COS detector. Boxcar source extraction was performed on rectangular apertures that include $\simeq 100\%$ of the flux of a point source in the covered wavelength range (i.e. accounting for COS’s astigmatism in the cross-dispersion direction) while minimizing the background contribution. For G140L spectra we chose a 25-pixel aperture at every LP, which for LP3 conveniently excludes the gain-sagged trace at the close-by LP1¹. For the G130M spectra of Q 0302–003 taken in the 1291 Å and 1318 Å setups we deemed a 23-pixel aperture as adequate, while the 1222 Å setup used in Program 12816 required 35 pixels due to its wider cross-dispersion profile.

The PHA range of the science data was determined from the two-dimensional count distribution in the trace (G130M) or from the fraction of geocoronal Ly α counts at a given PHA value (G140L), and is listed for every (re)analyzed target in Table 2. The PHA range determined from geocoronal Ly α extends to the lowest values encountered in the science data due to locally stronger detector gain sag, and includes $> 99\%$ of the total Ly α flux in the extraction aperture.

The dark current in the science aperture was estimated from post-processed dark monitoring exposures taken within ± 1.5 months around the date of observation (W16) at the same detector voltage and using the PHA range determined for the science exposures. Different time windows were adopted for Q 0302–003 and Q 1602+576 that were observed shortly before or after an increase of the detector voltage that interferes with the long-term dark monitoring. As detailed in W16, we coadded dark exposures taken in similar environmental conditions, as determined from the PHA distribution in two 50–60-pixel wide unilluminated windows above and below the science aperture. These included previous gain-sagged COS LPs, but that is inconsequential to our calibration efforts. The pulse-height-screened dark current extracted in the science aperture was smoothed by a 500-pixel running average and scaled to the total dark cur-

¹ We refrained from using the new TWOZONE extraction algorithm in CALCOS due to its inaccurate dark current estimation from offset windows with different gain sag characteristics. Moreover, TWOZONE is currently not applicable to dark exposures, and to data obtained at COS LPs 1 and 2.

Table 1. Sample of UV-bright $z_{\text{em}} > 2.7$ Quasars

Object	R. A. (J2000)	Decl. (J2000)	z_{em}	PID ^a	Instrument	R^b	t_{exp} (s)	S/N ^c	$f_{1500\text{\AA}}^d$	α^e	z_{abs}	$\log N_{\text{HI}}^f$	Ref. ^g
HS 1700+6416	17 ^h 01 ^m 00 ^s .61	+64°12′09″.1	2.751	11528	COS G140L	2000	15705	15	21.590	-1.756	0.8648	16.05	1
											0.7222	16.17	
											0.5528	15.87	
HS 1024+1849	10 ^h 27 ^m 34 ^s .13	+18°34′27″.5	2.860	12816	COS G130M	15000	28689	5	2.935	-0.560	2
Q 1602+576	16 ^h 03 ^m 55 ^s .92	+57°30′54″.4	2.862	12816	COS G130M	15000	15613	7	6.188	-2.463	2
HE 2347-4342	23 ^h 50 ^m 34 ^s .21	-43°25′59″.6	2.887	11528	COS G140L	2000	11557	14	20.325	-2.690	0.5766	< 15.8	1
					COS G130M	16000	28458	19			0.4215	< 15.8	
PC 0058+0215	01 ^h 00 ^m 58 ^s .39	+02°31′31″.4	2.89	11742	COS G140L	2000	6212	4	1.415	-1.289	1
SDSS J0936+2927	09 ^h 36 ^m 43 ^s .50	+29°27′13″.6	2.930	11742	COS G140L	2000	4739	4	1.086	-2.314	0.2121	blend	1
SDSS J0818+4908	08 ^h 18 ^m 50 ^s .01	+49°08′17″.0	2.957	11742	COS G140L	2000	7598	4	1.246	-2.295	0.2015	≤ 17.0	1
HS 1157+3143	12 ^h 00 ^m 06 ^s .24	+31°26′30″.8	2.989	9350	STIS G140L	1000	26820	11	0.541	-7.346	1
SDSS J0924+4852	09 ^h 24 ^m 47 ^s .35	+48°52′42″.8	3.027	11742	COS G140L	2000	7598	8	2.432	-2.085	0.4570	< 16.0	1
											0.2280	blend	
SDSS J1101+1053	11 ^h 01 ^m 55 ^s .74	+10°53′02″.3	3.029	11742	COS G140L	2000	7157	4	1.028	-2.953	0.3177	~ 16.5	1
											0.1358	21.13	
HE2QS J2157+2330	21 ^h 57 ^m 43 ^s .63	+23°30′37″.3	3.143	13013	COS G140L	1400	8074	4	5.772	-3.185	0.8092	17.27	2
											0.7112	16.96	
											0.5545	16.52	
SDSS J1237+0126	12 ^h 37 ^m 48 ^s .99	+01°26′07″.0	3.154	11742	COS G140L	2000	6212	4	1.401	-2.290	1
HE2QS J2321+1558	23 ^h 21 ^m 54 ^s .98	+15°58′34″.2	3.212	13013	COS G140L	1400	7427	0	6.427	-1.165	0.7572	17.11	2
											0.4900	~ 18.2	
HE2QS J1706+5904	17 ^h 06 ^m 21 ^s .74	+59°04′06″.4	3.248	13013	COS G140L	1400	15300	4	0.809	-1.152	0.6220	16.29	2
											0.4040	~ 18.5	
HE2QS J2149-0859	21 ^h 49 ^m 27 ^s .77	-08°59′03″.6	3.259	13013	COS G140L	1400	7561	3	0.928	-2.116	0.3530	< 16.5	2
Q 0302-003	03 ^h 04 ^m 49 ^s .85	-00°08′13″.5	3.286	12033	COS G130M	16000	24870	3	2.816	-3.534	2
HE2QS J0233-0149	02 ^h 33 ^m 06 ^s .01	-01°49′50″.5	3.314	13013	COS G140L	1400	7307	4	1.885	-2.074	0.3825	< 16.6	2
											0.3186	< 16.8	
HS 0911+4809	09 ^h 15 ^m 10 ^s .01	+47°56′58″.8	3.350	12816	COS G130M	15000	26864	6	3.034	-0.475	0.3028	< 16.8	2
											0.1827	~ 18.5	
HE2QS J0916+2408	09 ^h 16 ^m 20 ^s .85	+24°08′04″.6	3.440	13013	COS G140L	1400	7954	4	3.241	-2.117	0.6638	16.79	2
SDSS J1253+6817	12 ^h 53 ^m 53 ^s .71	+68°17′14″.2	3.481	12249	COS G140L	2000	14095	7	1.834	-2.858	0.6930	16.09	2
SDSS J2346-0016	23 ^h 46 ^m 25 ^s .66	-00°16′00″.4	3.512	12249	COS G140L	2000	20737	8	2.053	-1.771	2
HE2QS J2311-1417	23 ^h 11 ^m 45 ^s .46	-14°17′52″.1	3.705	13875	COS G140L	1600	11084	4	2.025	-2.600	0.7515	16.37	2
											0.4779	< 17.2	
SDSS J1137+6237	11 ^h 37 ^m 21 ^s .72	+62°37′07″.2	3.779	13875	COS G140L	1600	50993	4	0.509	-2.980	2
HE2QS J1630+0435	16 ^h 30 ^m 56 ^s .34	+04°35′59″.4	3.788	13013	COS G140L	1400	7908	4	3.397	-1.158	2
SDSS J1614+4859	16 ^h 14 ^m 26 ^s .81	+48°59′58″.8	3.812	13875	COS G140L	1600	28369	3	0.559	-2.472	2
SDSS J1711+6052	17 ^h 11 ^m 34 ^s .41	+60°52′40″.3	3.834	12249	COS G140L	2000	23951	4	1.467	-4.803	0.7750	16.53	2
											0.4370	≤ 18.0	
SDSS J1319+5202	13 ^h 19 ^m 14 ^s .20	+52°02′00″.1	3.930	12249	COS G140L	2000	26643	2	0.876	-5.767	0.7026	17.27	2

^a *HST* Program Number.^b Spectral resolution $R \equiv \lambda/\text{FWHM}$ at $\lambda = 1150 \text{ \AA}$.^c Signal-to-noise ratio per pixel (COS G140L: $\approx 0.24 \text{ \AA pixel}^{-1}$, COS G130M $R \approx 16000$: $\approx 0.03 \text{ \AA pixel}^{-1}$, COS G130M $R \approx 15000$: $\approx 0.04 \text{ \AA pixel}^{-1}$, STIS G140L: $0.6 \text{ \AA pixel}^{-1}$) near He II Ly α in the quasar rest frame. HE2QS J2321+1558 and HE2QS J1706+5904 are not considered further due to strong intervening H I Lyman limit systems.^d Continuum flux density at 1500 \AA in $10^{-16} \text{ erg cm}^{-2} \text{ s}^{-1} \text{ \AA}^{-1}$.^e Power-law spectral index α for $f_{\lambda} = f_{1500\text{\AA}} (\lambda/1500\text{\AA})^{\alpha}$ including a correction for identified H I Lyman continuum absorption.^f Logarithmic column density of identified intervening H I absorber in cm^{-2} .^g Data reference. 1: [Worseck et al. \(2016\)](#), 2: This paper.

Table 2. PHA Ranges Adopted for (Re)analyzed Quasars

Object	LP	Dates	Segment A	Segment B
SDSS J2346–0016	1	2010 Nov 29	2–15	...
	1	2010 Dec 4	2–15	...
SDSS J1711+6052	1	2011 Apr 27–28	2–15	...
	1	2011 Oct 9	1–14	...
SDSS J1319+5202	1	2011 May 4, 8	2–15	...
SDSS J1253+6817	1	2011 May 5	2–15	...
Q 0302–003	1	2012 Mar 8, 9	1–15	1–15
HS 1024+1849	2	2013 Mar 25, 26	3–14	3–14
HE2QS J1706+5904	2	2013 Apr 11	3–14	...
HE2QS J1630+0435	2	2013 Apr 12	3–14	...
HE2QS J2149–0859	2	2013 Apr 27	3–14	...
HS 0911+4809	2	2013 May 3, 5	3–14	3–14
HE2QS J2321+1558	2	2013 May 9	3–14	...
HE2QS J2157+2330	2	2013 Jul 19	2–13	...
Q 1602+576	2	2013 Jul 20	3–14	4–15
HE2QS J0233–0149	2	2013 Aug 7	2–13	...
HE2QS J0916+2408	2	2013 Dec 4	2–13	...
SDSS J1614+4859	3	2015 Aug 28, 31	2–14	...
SDSS J1137+6237	3	2015 Sep 17–18	2–14	...
	3	2015 Nov 10–11	2–14	...
HE2QS J2311–1417	3	2015 Nov 7	2–14	...

rent expected in the science exposure using the PHA calibration windows. Validation tests with dark exposures following W16 confirmed that the chosen 500-pixel averaging scale captured the large-scale spatial variations (up to a factor 2.8) in the Segment A dark current occurring around solar maximum. Together with more frequent dark monitoring beginning in Cycle 20 (65×1330 s in the considered 3-month window) this ensured percent-level accurate dark estimation in highly variable environmental conditions.

Open-shutter backgrounds were treated as in W16. In short, the quasi-continuous FUV sky background was taken from Murthy (2014). Earthshine was significant only for HE2QS J1706+5904, so for this target we restricted the limb angle to $> 21^\circ$ in the affected wavelength range 1142–1181 Å. Likewise, geocoronal emission lines (N I λ 1134 Å, N I λ 1200 Å, H I λ 1216 Å, N I λ 1243 Å, O I λ 1304 Å, O I λ 1356 Å) were suppressed using data restricted in solar altitude and/or limb angle. Residual geocoronal emission was flagged, in particular the remaining core of H I Ly α and the region around O I λ 1304 Å that has very little sensitivity to high He II absorption due to the reduced exposure time in orbital night. Scattered geocoronal Ly α emission in the G140L spectra was estimated from the recorded geocoronal Ly α flux and an empirical model describing its amplitude along the dispersion axis (W16). For HE2QS J2149–0859 and SDSS J1614+4859 that were observed mostly during orbital day (daytime fractions 79.8% and 83.7%, respectively) the uncertainty in our scattered light model dominates the total background uncertainty and results in appreciable negative flux on large scales, limiting the sensitivity to strong

He II absorption. Comparing data taken during orbital day and night we verified the presence of scattered geocoronal Ly α emission in the G130M spectra of Q 0302–003 and HS 0911+4809, and used only nighttime data in the affected wavelength range (≈ 10 Å around geocoronal Ly α). For HS 0911+4809 the cuts were more extensive to exclude strong geocoronal N I λ 1200 Å and very weak but present N I λ 1243 Å emission. Beyond that, saturated He II absorption confirms that scattered light is insignificant in G130M spectra.

Subexposures were coadded by summing the detected Poisson counts and the post-processed background on the CALCOS wavelength grid, accounting for varying pixel exposure times due to offsets in dispersion direction, detector blemishes, and geocoronal emission. Absorption lines in the quasar continuum and He II transmission features were used to verify the alignment of each individual grating setup across multiple visits. However, subexposures taken at different central wavelengths showed local distortions in the wavelength solution by up to several resolution elements (e.g. Wakker et al. 2015) that are probably caused by inaccuracies in the geometric distortion correction and detector walk (Sahnou et al. 2016). These local wavelength calibration errors do not affect our measurements of the mean He II absorption on scales $\Delta z \geq 0.01$, corresponding to $\gtrsim 4$ G140L and $\gtrsim 25$ G130M resolution elements, respectively.

The coadded counts were flux-calibrated using the time-dependent flux calibration curve determined by CALCOS. For targets observed in multiple visits or at several central wavelengths we used an exposure-time-weighted average calibration curve to preserve the Poisson count statistics. The G140L spectra were binned by a factor of three to yield a sampling of 2–3 0.24 Å pixels per resolution element in the wavelength range of interest (1100–1500 Å). The G130M spectra were binned to two pixels per resolution element accounting for the lower resolution of the 1222 Å setup, yielding dispersions of ≈ 0.03 Å pixel $^{-1}$ for Q 0302–003, and ≈ 0.04 Å pixel $^{-1}$ for the three quasars observed in Program 12816, respectively. The asymmetric Poisson error was calculated accounting for the background (Feldman & Cousins 1998). For plotting purposes we computed an approximate 1σ error array by adding in quadrature the larger of the asymmetric Poisson error and the propagated background error. Almost all G140L spectra obtained in our Cycle 20 and 22 programs reach a S/N ≈ 4 per 0.24 Å pixel near He II Ly α in the quasar rest frame (Table 1). The G130M spectra have a higher continuum S/N per Å due to their higher dispersion.

2.5. Continuum Definition

Since the intrinsic FUV flux of He II-transparent quasars is partially attenuated by low-redshift H I Lyman limit absorbers, many of which are in the NUV (e.g. Worseck & Prochaska 2011), one can only fit quasi-continua in the covered FUV spectral range that do not represent the intrinsic quasar spectral energy distributions. Their full reconstruction would require contiguous and near-simultaneous spectral coverage from the FUV to the optical to locate Lyman

limit breaks while minimizing uncertainties due to quasar variability (Syphers & Shull 2013; Syphers & Shull 2014). Moreover, due to the strong unresolved He II absorption in the G140L spectra it is necessary to extrapolate a continuum from redward of He II Ly α , including identified Lyman limit breaks in the covered spectral range.

We modeled the continuum as a power-law $f_\lambda \propto \lambda^\alpha$, accounting for Galactic extinction, low-redshift IGM and ISM absorption, weak quasar emission lines apparent in a few spectra, and residual geocoronal contamination. All spectra were corrected for Galactic extinction with their respective line of sight selective extinction $E(B - V)$ from Schlegel et al. (1998) and the Cardelli et al. (1989) extinction curve assuming the Galactic average ratio between total V band extinction and selective extinction $R_V = 3.1$. Each G140L spectrum was searched for (partial) Lyman limit absorbers identified by their Lyman series transitions, whose column densities were added as additional free parameters to the power-law continuum if the spectral range redward of the break improved the continuum fit. The power-law including Lyman limit breaks was fitted to select regions deemed free of emission and absorption lines redward of He II Ly α via a maximum likelihood routine, with continuum errors estimated by refitting Poisson deviates of the inferred continuum counts 10,000 times. Table 1 lists the continuum parameters and the identified Lyman limit systems for all quasars considered in this work, including nine quasars from W16 for completeness. For absorbers with inferred optically thin Lyman limit breaks overlapping with the He II absorption we obtained upper limits on the H I column densities from He II IGM transmission features. These potential breaks were not considered in the continuum fit, such that the He II absorption at shorter wavelengths may be overestimated by up to $\delta\tau_{\text{eff}} \simeq 1$ (HE2QS J2311–1417 in Table 1). Two quasars observed in our Cycle 20 survey have their FUV spectra truncated by intervening optically thick Lyman limit systems shortly redward (HE2QS J2321+1558) or blueward (HE2QS J1706+5904) of He II Ly α in the quasar rest frame (Table 1), and are not considered for further analysis². The different PHA cuts adopted for the quasars from Program 12249 did not significantly change their continuum fits reported in W16.

Since most G130M spectra have insufficient spectral coverage redward of He II Ly α for a reliable continuum extrapolation we adopted their respective G140L continua after correcting for quasar variability between the G140L and the G130M observations. Specifically, we measured the average fluxes in 20 Å bins in the overlapping spectral range redward of He II Ly α and determined their ratio to check for variations in the flux normalization and the spectral slope. The two $z_{\text{em}} = 2.86$ quasars from Program 12816 had enough spectral coverage redward of He II Ly α to rescale their Cy-

Table 3. Flux Ratio between FUV Spectra at different Epochs

Object	1st epoch	2nd epoch	Mean flux ratio (2nd/1st epoch)
Q 0302–003	1997 Dec 2, 10	2012 Mar 8, 9	0.90 ± 0.02
HS 0911+4809	2010 Oct 6–7	2013 May 3, 5	0.78 ± 0.01
HS 1024+1849	2011 Mar 14	2013 Mar 25, 26	0.59 ± 0.01
Q 1602+576	2011 Mar 4	2013 Jul 20	1.14 ± 0.01

cle 18 G140L spectra that were analyzed in W16. As the 1-orbit G140L exposures of Q 0302–003 and HS 0911+4809 taken together with the G130M spectra were of insufficient quality for a continuum fit, we used them only to determine the level of quasar variability compared to their earlier STIS and COS G140L spectra (W16). All four quasars were consistent with a constant flux ratio redward of He II Ly α , so for all quasars we adopted its mean to rescale the G140L continuum normalization, adding its standard error in quadrature to the statistical continuum error (Table 3). For HS 0911+4809 the 45 Å continuum overlap between the G130M and the G140L spectrum revealed a $\simeq 3\%$ inconsistency in the absolute flux calibration that was corrected by rescaling the G130M flux calibration curve.

3. EIGHT NEW SCIENCE-GRADE HE II QUASAR SIGHTLINES AT $Z > 3.1$

Six out of the eight targeted FUV-bright $z_{\text{em}} > 3.1$ quasars discovered in HE2QS do not show optically thick low- z H I Lyman limit absorbers, and qualify for a quantitative analysis of the He II Ly α absorption along their sightlines. Figure 1 shows their *HST*/COS G140L spectra together with our G140L follow-up spectra of two known He II-transparent SDSS quasars and our reductions of recent archival G130M data of four He II sightlines. Blueward of He II Ly α and the proximity zone of the background quasar (e.g. Zheng et al. 2015; Khrykin et al. 2016) we observe the redshift evolution of the intergalactic He II Ly α absorption. At $z > 3.5$ the He II absorption is ubiquitously saturated, with the exception of an isolated He II transmission spike at $z = 3.582$ in the sightline toward HE2QS J1630+0435. These spikes become more frequent and prominent at $3 < z < 3.3$, evolving into coherent structures of alternating patchy absorption at $z < 3$. At $z \lesssim 2.8$ the G130M spectra probe the emerging He II Ly α forest at the end of He II reionization.

Figure 2 compares the He II Ly α redshift coverage of the eight new science-grade He II sightlines reported here to the 17 sightlines presented in W16. Wavelength ranges with residual geocoronal emission, higher-order He II Lyman series absorption, interloping saturated H I Lyman continuum absorption, and the proximity zones of the background quasars have been excluded. Together with the two $z > 3.5$ archival sightlines discussed in W16 and reanalyzed here, our *HST* Cycle 20 and 22 programs provide the first statistically meaningful sample of 6 science-grade (continuum

² Due to the confusion of saturated He II absorption and optically thick H I Lyman continuum absorption one requires $S/N \gtrsim 3$ survey spectra to identify Lyman limit systems via their Lyman series.

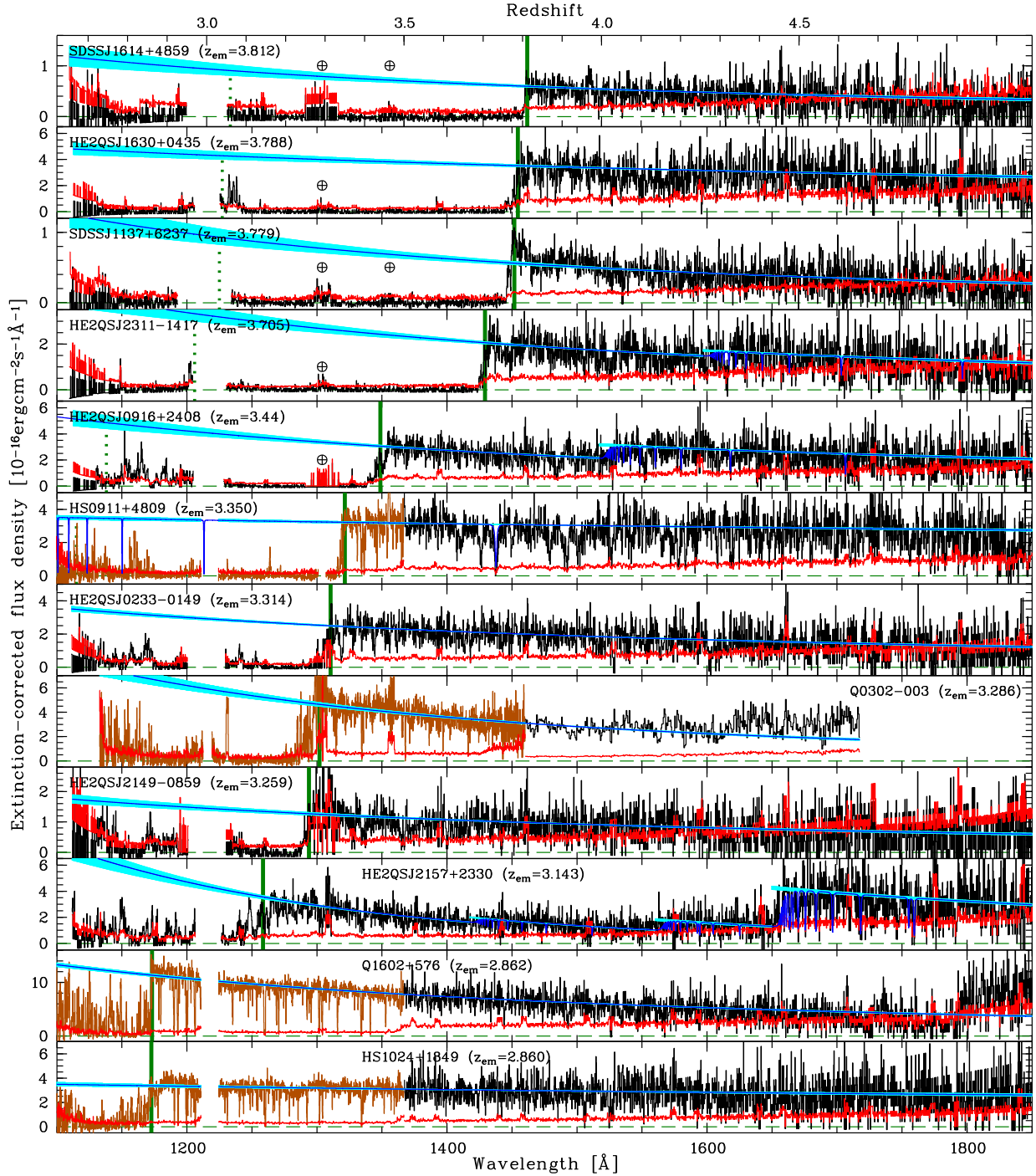


Figure 1. Extinction-corrected *HST* FUV spectra (black/brown) and corresponding 1σ error arrays (red) of 12 He II-transparent quasar sightlines with either new or significantly deeper data than presented in W16. The redshift axis (top) is for He II Ly α . Low-resolution spectra (black) have been taken with COS (G140L, $R = 1400\text{--}2000$ at 1150 \AA depending on the COS LP, binned to $0.24\text{ \AA pixel}^{-1}$) with the exception of Q 0302–003 for which we show its higher-quality STIS spectrum (G140L, $R \sim 1000$, $0.6\text{ \AA pixel}^{-1}$). COS G130M spectra are plotted in brown ($R = 15,000\text{--}16,000$ at 1150 \AA , binned to $0.12\text{ \AA pixel}^{-1}$ for display purposes), and the corresponding G140L spectra taken at different epochs have been rescaled to correct for quasar variability. The spectral region contaminated by geocoronal Ly α is not shown, and regions with residual O I emission have been marked (Earth symbols). The green dashed lines mark the zero level, whereas the green vertical lines mark He II Ly α (solid) and He II Ly β (dotted) in the quasar rest frame. The blue lines show power-law continuum fits to absorption-free regions redward of He II Ly α and the corresponding 1σ error (cyan shaded). For four quasars (HE2QS J2311–1417, HE2QS J0916+2408, HS 0911+4809, and HE2QS J2157+2330) the power-law continua include identified Lyman series and continuum absorption from intervening low-redshift H I Lyman limit systems (Table 1), convolved to COS resolution.

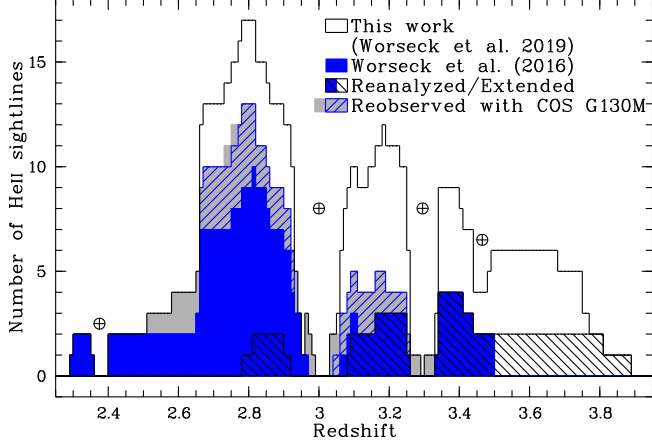


Figure 2. Redshift coverage of the present He II quasar sample (black) compared to our previous study at $z < 3.5$ (blue; W16). The black hatched histogram shows the redshift coverage of four $z_{\text{em}} > 3.4$ quasars with reanalyzed *HST*/COS data. Four quasars have been reobserved with the *HST*/COS G130M grating, extending their redshift coverage (gray vs. blue hatched). Earth symbols mark redshift ranges impacted by geocoronal emission.

$S/N \approx 4$) He II sightlines at $z > 3.5$. The total redshift pathlength $g(z > 3.5) = \sum_{z > 3.5} \Delta z$ is 1.65. In W16 we focused on $z < 3.5$ due to the limited sample size and decreasing instrument sensitivity at higher redshifts, providing the first statistical analysis of He II absorption at $3 < z < 3.5$ and a sizeable sample of ~ 10 He II sightlines at $2.7 < z < 3$. With four new $z_{\text{em}} > 3.5$ quasars and a quasar at $z_{\text{em}} = 3.44$ we more than double the redshift pathlength at $3.3 < z < 3.5$ from 0.50 to 1.16. At redshifts $3 < z < 3.3$ the increase is even larger ($g(3 < z < 3.3) = 2.04$ vs. 0.83 in W16) due to the two additional $z_{\text{em}} \approx 3.3$ He II-transparent quasars discovered in HE2QS.

The COS G130M spectra of the four previously known He II sightlines provide higher sensitivity to probe saturated He II absorption than their existing low-resolution COS and STIS spectra. At G130M resolution ($R \sim 15,000$) most He II transmission spikes are resolved, enabling detailed studies of the small-scale patchiness of the He II absorption. Moreover, the eight times higher dispersion of the G130M compared to the G140L results in an eight times narrower spectral range contaminated by geocoronal emission, allowing one to probe He II absorption in otherwise inaccessible redshift ranges at $z \sim 3$ and $z \sim 3.3$. In addition, the G130M 1222 Å setup extends the spectral coverage to $z < 2.66$, i.e. outside the spectral range of the G140L 1105 Å setup.

4. THE REDSHIFT EVOLUTION OF THE HE II EFFECTIVE OPTICAL DEPTH

4.1. Measurement Technique

To quantify the level of He II absorption in our mostly Poisson-count-limited spectra we employed the same technique as in W16, which we briefly summarize here. We computed the effective optical depth $\tau_{\text{eff}} = -\ln \langle f_{\lambda}/E_{\lambda} \rangle$, where

f_{λ} is the observed flux density, E_{λ} is the extrapolated quasar continuum, and $\langle \rangle$ denotes the average taken over a redshift range Δz . As in W16 we adopted regular regular redshift bins of common size $\Delta z = 0.04$, corresponding to ≈ 44 (≈ 30) cMpc at $z = 2.7$ ($z = 3.8$) in our assumed cosmology. The chosen bin size mainly preserves the sensitivity to high τ_{eff} values at $z > 3$, while the fixed bin centers ensure an objective comparison of the sightlines without focusing on individual features. Moreover, large-scale structures are not highly correlated on ≈ 40 cMpc scales, such that the measurements along a sightline can be treated as independent³. For each sightline, redshift bins with incomplete spectral coverage $g(z)$ were excluded (Figure 2), yielding a sample of 206 $\Delta z = 0.04$ redshift bins.

In each redshift bin, τ_{eff} was computed by maximizing the Poisson likelihood function

$$L = \prod_{j=1}^k \frac{(S_j + B_j)^{N_j} e^{-(S_j + B_j)}}{N_j!} \quad (1)$$

of k contiguous pixels with an integer number of registered counts N_j , the post-processed multi-component background B_j , and the unknown signal S_j . The signal was modeled as a constant in He II transmission, converted to non-integer source counts via the pixel exposure time t_j , the extinction-corrected flux calibration curve C_j , and the continuum E_j as

$$S_j = t_j C_j E_j e^{-\tau_{\text{eff}}} \quad (2)$$

For our rebinned COS spectra $\Delta z = 0.04$ corresponds to $k = 51$ G140L pixels, and 406 (305) pixels in the standard (1222 Å) G130M settings, respectively. Confidence intervals (1σ , 68.26% confidence) were computed via ordering the Poisson likelihood ratio (Feldman & Cousins 1998). If the He II transmission was formally negative or if the upper confidence limit included $\tau_{\text{eff}} = \infty$ we adopted the 1σ lower limit on τ_{eff} as a proxy for the sensitivity limit of our measurement, computed from 200,000 Poisson deviates of the background at zero source flux. Likewise, we estimated the significance of each τ_{eff} measurement by computing the probability

$$P(> N|B) = 1 - \sum_{k=0}^N \frac{B^k e^{-B}}{k!} \quad (3)$$

of having measured more than $N = \sum_j N_j$ counts just from the total background $B = \sum_j B_j$. Very small P values correspond to a statistically significant signal ($N \gg B$), whereas downward Poisson background fluctuations with $N \ll B$ result in $P \rightarrow 1$. The 1σ lower limit on τ_{eff} corresponds to $P = 0.1587$.

³ On smaller scales the density field and possibly also the radiation field exhibit progressively larger correlations. Repeating the statistical comparison to models of the He II-ionizing background (Section 5) with a scale $\Delta z = 0.01$ – but accounting for the expected correlations by sampling sightlines with four consecutive $\Delta z = 0.01$ bins per $\Delta z = 0.04$ segment – does not change our results.

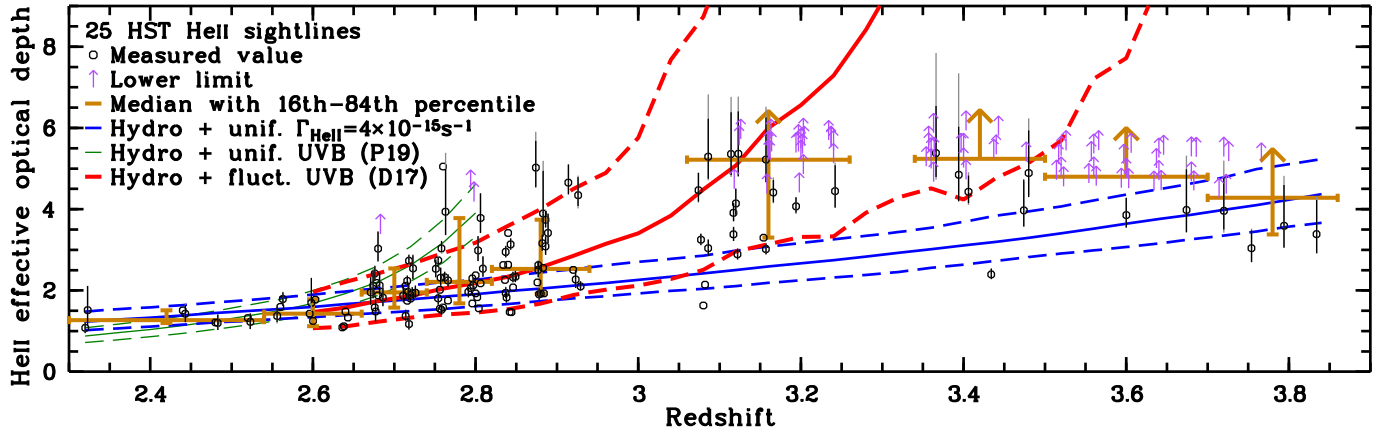


Figure 3. He II effective optical depth τ_{eff} vs. redshift for 25 He II sightlines in identical redshift bins of $\Delta z = 0.04$ (≈ 40 cMpc at $z = 3$), measured in the newly observed spectra (Fig. 1) or previously reported in W16. Measurements are plotted as black circles with error bars distinguishing statistical errors due to Poisson count statistics (black, double-sided 1σ errors corresponding to a confidence level of 68.26%) and estimated systematic errors from background uncertainties (gray). For clarity, the data are plotted slightly offset with respect to the identical bin centers and total error bars smaller than the symbol size have been omitted. If the upper confidence limit includes $\tau_{\text{eff}} = \infty$ or if the mean transmission is formally negative ($P > 0.1587$), we adopt the 1σ lower limit on τ_{eff} given by our instrumental sensitivity limit (arrow symbols). We also show the median τ_{eff} in subsamples in larger redshift intervals (brown), with the error bar indicating the 16th and the 84th percentile of the τ_{eff} distribution in the subsample. Overplotted are predictions from three UV background models applied to the Nyx hydrodynamic simulation output in the same $\Delta z = 0.04$ redshift bins (solid: median τ_{eff} ; dashed: 16th and 84th percentile): A model with a constant He II photoionization rate $\Gamma_{\text{HeII}} = 4 \times 10^{-15} \text{ s}^{-1}$ (thick blue), an evolving but uniform $\Gamma_{\text{HeII}}(z)$ applicable at $z \lesssim 2.8$ (thin green, Puchwein et al. 2019), and a fluctuating UV background model (thick red, Davies et al. 2017).

For each τ_{eff} measurement, background subtraction errors were incorporated as a systematic error estimated by Monte Carlo simulations, drawing 200,000 Gaussian deviates from the background including its estimated relative uncertainty of 2–14% depending on the orbit parameters and the environmental conditions during the observations (W16). With the inferred τ_{eff} for the modified background we generated a mock data sample by drawing from the Poisson distribution of the background and the inferred signal. Measuring τ_{eff} on these mock samples yielded an estimate of the total error from statistical Poisson shot noise and systematic background error. Accounting for the background uncertainties marginally increases the fraction of sensitivity lower limits on τ_{eff} from 34.5% to 36.9% in the sample. Significant detections with $P \ll 0.01$ are not affected by background uncertainties, and because of the object-to-object variations in the background uncertainties we did not compute formal errors on P . Given the strong He II absorption ($\tau_{\text{eff}} \gtrsim 1.5$), absorption lines from species other than He II and the statistical continuum error do not significantly add to the error budget, while systematic continuum error was minimized by excluding regions with uncertain interloping low- z H I Lyman continuum absorption.

4.2. Observational Results

Figure 3 presents the 206 τ_{eff} measurements or limits thereof in the 25 He II-transparent sightlines of our combined sample (Table 1). The 149 values for the 16 sightlines with either new or reanalyzed spectra are reported in Appendix A, while the remainder (9 sightlines marked in Table 1) has been taken from W16. With the eight new sightlines from our

HST programs in Cycle 20 and 22, and the extended spectral coverage of the recent COS G130M spectra we increase the $z < 3.5$ sample from W16 by 63% (168 vs. 103 τ_{eff} values). Thirty-eight newly reported τ_{eff} values provide the first statistical sample of quantified He II absorption at $z > 3.5$.

The He II effective optical depth increases with redshift, but with significant sightline-to-sightline variance at $z > 2.7$ that increases with redshift (W16). To quantify this, we computed the median τ_{eff} and its scatter (estimated from the range between the 16th and the 84th percentile) in larger redshift ranges, each having $n \gtrsim 20$ τ_{eff} values except at the lowest and highest redshifts. Note that for all following statistical analyses and data modeling (Section 5) we excluded the single remaining STIS spectrum of our sample (HS 1157+3143), since the STIS background uncertainties have been characterized to a lesser extent than for COS. Given the large redshift path, the exclusion of its four $z < 3$ τ_{eff} values does not change our results.

The results are plotted in Figure 3 in brown and are listed in Table 4. Table 4 also lists the error on the median that has been determined from the 16th and the 84th percentile of the distribution of the median τ_{eff} in 1000 bootstrap samples. In Table 5 we give the empirical cumulative distributions $F(< \tau_{\text{eff}})$ in these redshift ranges for the 24 HST/COS sightlines. Lower limits on τ_{eff} are included, such that the cumulative distributions represent a lower limit on the actual spread.

Redshifts $z < 2.66$ are covered by a maximum of four sightlines, limiting the robustness of the estimated scatter in τ_{eff} and the error on its median. At $2.66 < z < 2.74$ we observe a narrow τ_{eff} distribution around $\tau_{\text{eff}} \approx 2$ sampled

Table 4. 50th, 16th and 84th percentiles of the τ_{eff} distribution in subsamples of n values in m *HST*/COS He II sightlines

Δz	n	m	$\tau_{\text{eff},50}$	$\tau_{\text{eff},16}$	$\tau_{\text{eff},84}$
2.30–2.54	8	2	$1.27^{+0.10}_{-0.06}$	1.20	1.51
2.54–2.66	11	4	$1.43^{+0.17}_{-0.10}$	1.12	1.78
2.66–2.74	24	13	$1.95^{+0.09}_{-0.06}$	1.58	2.54
2.74–2.82	28	15	$2.21^{+0.10}_{-0.15}$	1.68	3.78
2.82–2.94	28	13	$2.53^{+0.10}_{-0.20}$	1.92	3.74
3.06–3.26	42	13	> 5.22	3.30	...
3.34–3.50	23	9	> 5.24	> 4.68	...
3.50–3.70	29	6	> 4.80	> 4.47	...
3.70–3.86	9	5	> 4.28	3.38	...

by 24 $\Delta z = 0.04$ bins in 13 sightlines. Given that the subsample contains only one τ_{eff} sensitivity limit, the scatter in τ_{eff} is well determined. At $z > 2.74$ the median τ_{eff} gradually increases and its scatter doubles with respect to the data at $z \approx 2.7$. Our new He II sightlines have the lowest τ_{eff} measured in 13 COS sightlines at $z = 2.84$ ($\tau_{\text{eff}} = 1.47 \pm 0.05$ toward HE2QS J0916+2408 and $\tau_{\text{eff}} = 1.47^{+0.07}_{-0.06}$ toward HE2QS J0233–0149). At the other extreme we obtain $\tau_{\text{eff}} > 4.19$ at $z = 2.80$ in the HE2QS J2149–0859 sightline, confirming the result of W16 that the sightline-to-sightline variance in He II absorption increases between $z \approx 2.7$ and $z \approx 2.8$.

At $z > 3$ the τ_{eff} distribution is affected by frequent sensitivity limits to high values $\tau_{\text{eff}} \approx 5$. In each $z > 3$ subsample the median τ_{eff} corresponds to a sensitivity limit, and therefore the true median τ_{eff} is underestimated. At $3.06 < z < 3.26$ the 16th percentile of the distribution is still well determined due to the remaining tail toward low τ_{eff} and the large sample size. The tail toward low τ_{eff} is more than a factor of three larger than at $z \approx 2.9$, indicating a significant increase in the τ_{eff} scatter at $z > 3$. Figure 4 shows the spectra of nine He II sightlines covering $3.06 < z < 3.26$, seven of which are new, while two (Q 0302–003 and HS 0911+4809) have significantly deeper COS G130M data than the low-resolution STIS and COS data analyzed in W16. Several sightlines show significant He II transmission spikes that are much narrower ($\Delta z \lesssim 0.01$ or $\Delta v \lesssim 720 \text{ km s}^{-1}$) than our chosen bin size $\Delta z = 0.04$, but limited S/N prevents a robust characterization of their size distribution. Since we observe strong saturation between them, these transmission spikes are robust to residual background subtraction systematics. In the HS 0911+4809 sightline the new G130M data confirm the three most significant $z > 3$ transmission features ($P < 0.01$) detected in the G140L data (W16), although the $z \approx 3.07$ spike is weaker, probably due Poisson noise in the G140L data. In our new sightlines we find the three lowest τ_{eff} values at $3.06 < z < 3.26$ (HE2QS J1630+0435: $\tau_{\text{eff}} = 1.63 \pm 0.06$ at $z = 3.08$; HE2QS J0233–0149: $\tau_{\text{eff}} = 2.14^{+0.08}_{-0.09}$ at $z = 3.08$ and $\tau_{\text{eff}} = 2.89^{+0.14}_{-0.13}$ at $z = 3.12$). HE2QS J2149–0859 and SDSS J1614+4859 – the two spectra that were observed

Table 5. Cumulative distributions of τ_{eff} in redshift ranges

z_{min}	z_{max}	τ_{eff}	$F(< \tau_{\text{eff}})$	Flag ^a
2.30	2.54	1.08	0.000	0
2.30	2.54	1.20	0.125	0
2.30	2.54	1.21	0.250	0
2.30	2.54	1.23	0.375	0
2.30	2.54	1.32	0.500	0

^aFlag indicating whether the τ_{eff} value is a measurement (0) or a 1σ upper limit (1).

NOTE—Table 5 is published in its entirety in the machine-readable format. A portion is shown here for guidance regarding its form and content.

mostly during orbital day – show significantly negative transmission on large scales, indicating that the simple model developed in W16 may overestimate the scattered geocoronal Ly α emission by $\sim 20\%$, but our results remain unaffected by this uncertainty⁴.

At $z > 3.3$ the tail toward well determined low τ_{eff} values gradually disappears. The fraction of robust ($P < 0.1587$) τ_{eff} measurements decreases from 42.9% at $3.06 < z < 3.26$ to 26.1% at $3.34 < z < 3.5$ at similar sensitivity, suggesting that the actual median τ_{eff} is significantly higher than our sensitivity limit. With more than twice the pathlength than in W16 we obtain a significantly lower fraction of robust τ_{eff} measurements at $3.34 < z < 3.5$ (26.1% vs. 50%), indicating strong sightline-to-sightline variance in the He II absorption. Figure 5 focuses on the $z > 3.3$ He II absorption spectra of the 6 $z_{\text{em}} > 3.5$ quasars including the reanalyzed sightlines of SDSS J1319+5202 and SDSS J1711+6052. In W16 we reported on the strong transmission spike at $z \approx 3.45$ in the SDSS J1319+5202 sightline. A narrower and weaker, but still significant ($P = 2.17 \times 10^{-4}$) spike occurs in the sightline to HE2QS J1630+0435 at $z = 3.582$. Note that P is even smaller ($P < 10^{-7}$ eventually limited by background uncertainty) across the observed width of the spike ($3.58 < z \lesssim 3.59$, $\Delta v \lesssim 650 \text{ km s}^{-1}$). At $z > 3.4$ several sightlines show unresolved narrow transmission features of single 0.24 \AA pixels. Although formally significant ($P \lesssim 0.001$ for single pixels), these could also be rare background events, and more or higher-resolution data are required to confirm them. Otherwise most spectra are saturated on large scales or appear to be affected by background oversubtraction (SDSS J1614+4859). At $z > 3.5$ we obtain sensitivity limits $4.3 \lesssim \tau_{\text{eff}} \lesssim 5.4$ in 84.2% of the pathlength,

⁴ We tested this by varying the estimated scattered light for the 22 redshift bins at $3.06 < z < 3.26$ covered by COS G140L data that have insignificant He II transmission (i.e. $P \geq 0.1587$ and an adopted τ_{eff} sensitivity limit). A 20% reduction in the scattered light results in nominally positive transmission in about half of them (12/22), but in only three of them the detection is significant ($P < 0.1587$). This confirms that our procedure to adopt the 1σ lower limit on τ_{eff} guards against possible background systematics.

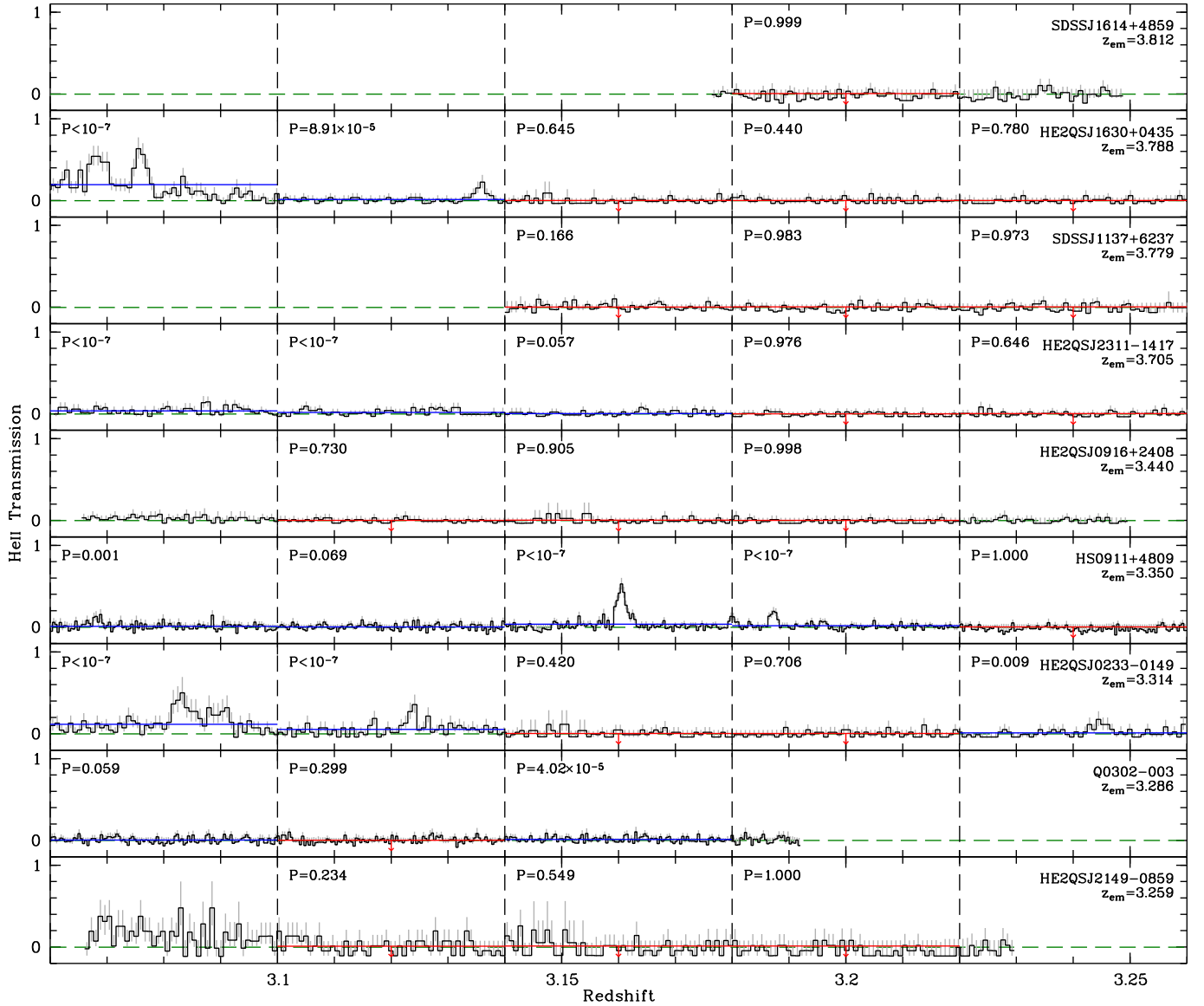


Figure 4. He II Ly α transmission spectra of nine quasar sightlines at $z \approx 3.16$ (black) with Poisson errors for individual pixels (gray). We only show spectra that have not been analyzed in W16 (Table 1). The COS G130M spectra of HS 0911+4809 and Q 0302–003 have been binned to $\approx 0.12 \text{ \AA pixel}^{-1}$ (0.7–0.9 pixels per resolution element). The COS G140L spectra of the remaining 7 sightlines have been binned to $\approx 0.24 \text{ \AA pixel}^{-1}$ (3 pixels per resolution element). The proximity zones of the background quasars and regions contaminated by geocoronal Ly α and residuals of geocoronal O I $\lambda 1304 \text{ \AA}$ emission have been omitted. The dashed horizontal lines mark the zero level, while the vertical lines indicate our regular $\Delta z = 0.04$ bins for our τ_{eff} measurements. The τ_{eff} measurements are overplotted, converted to the mean He II transmission, distinguishing robustly measured values (blue; measurement error comparable to the line thickness) and sensitivity limits (red with arrow symbols). Incompletely covered redshift bins were not considered. For every redshift bin we indicate the probability P that the measured mean He II transmission is consistent with a Poisson fluctuation of the background.

mostly due to the declining sensitivity of the G140L grating (Figure 3).

An exception to this trend is the SDSS J1319+5202 sightline, in which low-level He II transmission is detected in 3/4 $\Delta z = 0.04$ bins at $z > 3.7$. Combining these three redshift bins, the probability that the transmission at $3.74 < z < 3.86$ arises from a Poisson background fluctuation is very small ($P = 1.2 \times 10^{-4}$). Large-scale background undersubtraction in this particular sightline is unlikely due to insignifi-

cant or slightly negative transmission in 5/9 $z > 3.5$ redshift bins. Specifically, a factor of three increase in the modeled scattered geocoronal Ly α emission or a 17% increase in the dark current would render the transmission at $3.74 < z < 3.86$ insignificant ($P = 0.16$), but would result in unphysical strongly negative transmission in adjacent redshift bins. Also, the required increases in these background components are much larger than their estimated relative uncertainty ($\sim 18\%$ for the scattered light and 1.2% for the dark

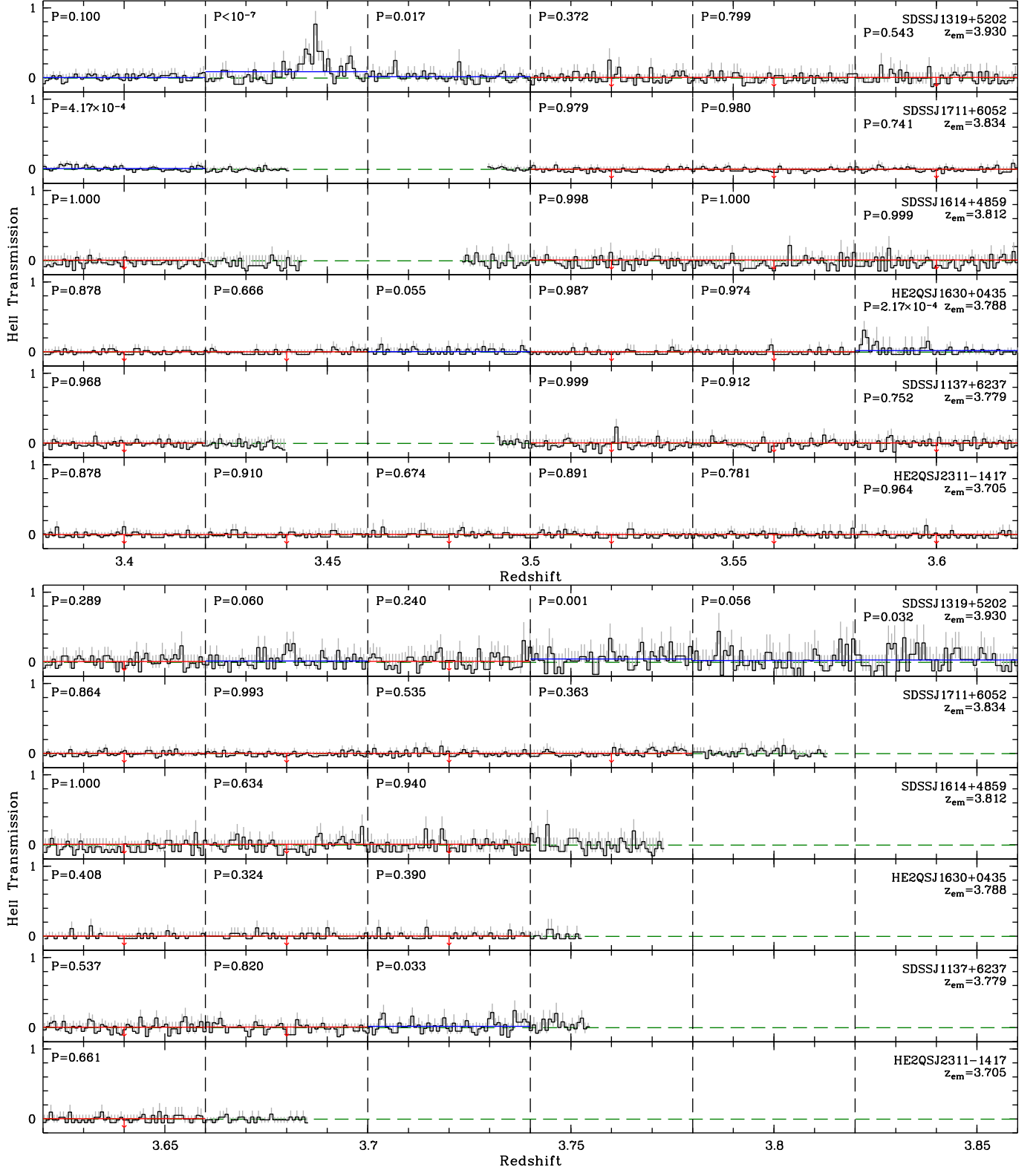


Figure 5. Similar to Figure 4, but showing the redshift ranges $3.36 < z < 3.62$ (upper panels) and $3.62 < z < 3.86$ (lower panels) for the 6 $z_{em} > 3.5$ quasars (Table 1). The spectra have been binned to 2–3 pixels per resolution element ($\approx 0.24 \text{ \AA pixel}^{-1}$). Occasional geocoronal O I $\lambda 1356 \text{ \AA}$ emission has been omitted.

current). The shadow data of SDSS J1319+5202 (58.6% of the total exposure at a scattered light level reduced by $\approx 80\%$) give consistent results within the necessarily larger errors ($P = 3.6 \times 10^{-3}$ at $3.74 < z < 3.86$). We conclude that the low-level He II transmission in the SDSS J1319+5202 sightline is likely real. Similar to lower redshifts, this transmission may be dominated by narrow spikes, but the data quality is particularly low due to the degrading sensitivity of the COS G140L grating and the low continuum flux of the background quasar. Note that the detected transmission at $z < 3.86$ is unlikely to be affected by the background quasar, because the proximity zones of $z = 3.9$ quasars rarely exceed 50 cMpc for a range of quasar lifetimes and ambient IGM He II fractions (Khrykin et al. 2016, 2019).

In summary, the He II effective optical depth increases from $\tau_{\text{eff}} \approx 2$ at $z \approx 2.7$ to $\tau_{\text{eff}} > 5$ at $z > 3$ with an intrinsic scatter that increases with redshift and indications of large-scale sightline-to-sightline variance. At $z > 3.5$ the 6 robust values at $\tau_{\text{eff}} \lesssim 4$ probe the low tail of the intrinsic τ_{eff} distribution, but our results are still limited by sample size and sightline variance. Narrow $\Delta z \lesssim 0.01$ He II transmission patches may exist even at $z > 3.5$, only a few of which are robustly detected at the current data quality.

5. THE HE II-IONIZING BACKGROUND

After having measured the redshift evolution of the He II effective optical depth and its scatter, we seek to compare our measurements to realistic mock τ_{eff} distributions from outputs of numerical hydrodynamical IGM simulations. Considering the large fraction of robust τ_{eff} measurements out to $z = 3.8$ and the saturation limit of the data at He II fractions of a few percent, we take the simplifying approach that our measurements probe the post-reionization IGM that is in photoionization equilibrium with a He II-ionizing background that may exhibit spatial fluctuations on large scales ($\gtrsim 20$ cMpc). Comparisons to detailed numerical radiative transfer simulations of quasar-driven He II reionization are left for future work.

5.1. Nyx Cosmological Hydrodynamical Simulation

To compare our τ_{eff} measurements to predictions for a range of UV background models we used outputs of a cubic $(100h^{-1} \text{ cMpc})^3$ hydrodynamical simulation performed with the Nyx code (Almgren et al. 2013; Lukić et al. 2015). Eulerian hydrodynamics of the baryons was computed on a fixed Cartesian grid with 4096^3 cells, and the evolution of dark matter was followed with 4096^3 Lagrangian particles. The spatial resolution of $25h^{-1} \text{ ckpc}$ is sufficient to resolve the H I and He II Ly α forest, and to reach convergence in H I Ly α transmission statistics to percent-level accuracy (Lukić et al. 2015). The simulation was run without adaptive mesh refinement, star formation or thermal feedback prescription, and is therefore optimized to resolve underdense regions in the IGM where much of the He II Ly α absorption originates (Croft et al. 1997; Theuns et al. 1998; McQuinn et al. 2009; Compostella et al. 2013). Convergence tests on $(20h^{-1} \text{ cMpc})^3$ volumes indicate that our fiducial simulation overestimates

the He II effective optical depth by $\sim 5\%$ (Appendix B). Primordial ideal gas chemistry (mass fractions $X = 0.76$ for H and $Y = 0.24$ for He) was computed assuming photoionization equilibrium in the optically thin limit, using the spatially uniform but redshift-dependent photoionization and photoheating rates by Haardt & Madau (2012).

We used the density, velocity and temperature fields of the seven outputs in the redshift range of interest ($z_{\text{sim}} = 2.2, 2.4, 2.5, 2.6, 3, 3.5, 4$). We extracted $\Delta z = 0.08$ skewers along one axis of the simulation volume, starting from random positions and applying periodic boundary conditions. To match the regular $\Delta z = 0.04$ grid of the τ_{eff} measurements we rescaled the density field along each skewer as

$$\rho(z) = \rho_{\text{sim}} \left(\frac{1+z}{1+z_{\text{sim}}} \right)^3, \quad (4)$$

and extracted 1000 skewers from the closest two Nyx outputs spaced by Δz_{sim} . For each redshift bin centered on z_{bin} the number of skewers from the two considered Nyx outputs was weighted with a factor $w = 1 - |z_{\text{sim}} - z_{\text{bin}}| / \Delta z_{\text{sim}}$. Ly α optical depths of H I and He II were computed accounting for peculiar velocities and thermal broadening (see e.g. Lukić et al. 2015 for details). Each $\Delta z = 0.08$ skewer comprised 2431 pixels, corresponding to a pixel scale of 3 km s^{-1} at $z = 2.3$ and 2 km s^{-1} at $z = 3.8$. To approximately account for the lack of strong H I Lyman limit systems in the observed He II sightlines (Compostella et al. 2014; W16) we discarded the 4–7% of skewers in which pixels reached $\tau_{\text{HI}} > 3000$, corresponding to H I column densities $N_{\text{HI}} \gtrsim 10^{17.1} \text{ cm}^{-2}$. In the observed He II sightlines the N_{HI} limit may be somewhat higher if there are no strong Lyman limit systems at $z \ll z_{\text{bin}}$ along the lightcone. Eventually, 900 of the 1000 skewers at each z_{bin} were kept.

5.2. UV Background Models Applied to the Nyx Skewers

5.2.1. Uniform UV Background Models

A posteriori, we linearly rescaled the He II Ly α optical depths to match the observed range in τ_{eff} . This rescaling adjusts the He II photoionization rate Γ_{HeII} in the optically thin limit ($\tau_{\text{HeII}} \propto \Gamma_{\text{HeII}}^{-1}$), but in reality also depends on the thermal state of the gas during and after He II reionization that the Nyx simulation does not follow self-consistently. We explore the impact of this approximation in Section 6.3 below. Changes in the ionization rate by a factor ~ 2 result in percent level errors in the transmission probability distribution and power spectrum at $z > 2$ (Lukić et al. 2015; Oñorbe et al. 2017). The much larger systematic effects of a fixed thermal history under photoionization equilibrium are explored in Section 6.3. Across the redshift range of interest we applied a range of constant He II photoionization rates $\Gamma_{\text{HeII}} = 10^{-15.3} - 10^{-14} \text{ s}^{-1}$ to the $\Delta z = 0.08$ skewers. Additionally, we mimicked a totally opaque IGM by multiplying all He II optical depths by a factor of 1000 (i.e. $\Gamma_{\text{HeII}} \approx 0$).

We also considered the spatially uniform but redshift-dependent UV background synthesis model by Puchwein et al. (2019) that consistently traces the overall thermal and

ionization history via one-dimensional radiative transfer in a three-phase medium. Since the Nyx simulation assumes photoionization equilibrium, we used the Puchwein et al. (2019) equivalent-equilibrium He II photoionization rates, interpolated onto our redshift bins. For simplicity we did not rescale the Nyx gas temperatures to the to those predicted by Puchwein et al. (2019), such that $\tau_{\text{eff}}(z)$ is not predicted self-consistently. We mainly aim to check whether a redshift-dependent uniform Γ_{HeII} is consistent with our data.

5.2.2. The D17 Fluctuating UV Background Model

Recently, D17 presented a three-dimensional model of a spatially fluctuating He II-ionizing background produced by scarce bright $z \sim 3$ quasars and a spatially varying mean free path of He II-ionizing photons. The model broadly reproduces the large τ_{eff} variations reported in W16. Hence, spatial fluctuations of the He II-ionizing UV background in a post-reionization IGM may be a viable alternative explanation to still ongoing He II reionization at $2.7 < z < 3$ (Worseck et al. 2011; W16).

We used the default model parameters from D17: A cubic $(500 \text{ cMpc})^3$ volume was randomly populated with quasars according to the Hopkins et al. (2007) luminosity function, each emitting isotropically at a constant luminosity for a fixed lifetime of 50 Myr. Approximate three-dimensional radiative transfer of He II-ionizing photons was calculated in grid cells of $(7.8 \text{ cMpc})^3$, modestly improved compared to the $(10 \text{ cMpc})^3$ resolution in D17, with outputs every 5 Myr, accounting for a spatially varying mean free path computed assuming local photoionization equilibrium. The IGM was approximated as an ensemble of randomly distributed discrete absorbers drawn from the Prochaska et al. (2014) column density distribution function. While this model certainly simplifies the absorber physics and captures UV background fluctuations only on scales larger than the mean free path ($\gtrsim 20 \text{ cMpc}$), D17 estimate that volumes $\gtrsim (500 \text{ cMpc})^3$ are required to reach convergence in the distribution of τ_{eff} on scales $\Delta z = 0.04$ to better than 10% at $z \lesssim 3$. Current cosmological simulations with more accurate radiative transfer still lack the required box size to capture the large-scale fluctuations and/or the spatial resolution to resolve transmission in the He II Ly α forest (Compostella et al. 2013, 2014; La Plante et al. 2017).

We applied the fluctuating UV background rates to the Nyx skewers by drawing $2.5 < z < 4$ lightcone skewers from the simulation volume, and rescaling the He II Ly α optical depths from the Nyx skewers ($\tau_{\text{HeII}} \propto \Gamma_{\text{HeII}}^{-1}$) in the overlapping redshift range without interpolating $\Gamma_{\text{HeII}}(z)$ between time steps.

5.2.3. The Predicted Redshift Evolution of the He II Effective Optical Depth

In Figure 3 we compare our τ_{eff} measurements to predictions from the 900 skewers per rescaled Nyx simulation snapshot, applying three UV background models described above: (1) a uniform constant $\Gamma_{\text{HeII}} = 4 \times 10^{-15} \text{ s}^{-1}$, (2) the uniform but redshift-dependent UV background model

from Puchwein et al. (2019), and (3) the fluctuating UV background model from D17. We show the redshift evolution of the median τ_{eff} and its scatter, estimated from the 16th and 84th percentiles of the τ_{eff} distribution on our adopted scale $\Delta z = 0.04$.

Among the uniform UV background models with a constant He II photoionization rate, the one with $\Gamma_{\text{HeII}} = 4 \times 10^{-15} \text{ s}^{-1}$ roughly matches the τ_{eff} measurements at $z \lesssim 2.6$, i.e. in the post-reionization He II Ly α forest. In this model, the shallow redshift evolution of the median He II effective optical depth from $\tau_{\text{eff},50} \simeq 1.3$ at $z = 2.3$ to $\tau_{\text{eff},50} \simeq 4$ at $z = 3.8$ is entirely due to density evolution in the IGM. Density fluctuations on the scale $\Delta z = 0.04$ give rise to a relative scatter of $\simeq 18\%$ around the median τ_{eff} that only slightly evolves with redshift. The observed scatter in τ_{eff} is much larger, indicating redshift evolution and/or spatial fluctuations in Γ_{HeII} . Nevertheless, the predicted range in τ_{eff} matches the locus of the lowest measured τ_{eff} values at all redshifts. These likely correspond to fully reionized regions in the IGM. However, at $z > 3.5$ it is increasingly difficult to distinguish such regions from saturated He II Gunn-Peterson troughs due to density evolution in the IGM and the sensitivity limit of the data.

Puchwein et al. (2019) use a quasar emissivity model and an empirical IGM absorber model to predict the redshift evolution of the average Γ_{HeII} and the corresponding τ_{eff} in the post-reionization IGM. In their model He II reionization completes at $z \simeq 2.8$, and Γ_{HeII} increases by a factor ~ 6 from $z = 2.75$ to $z = 2.3$, corresponding to a strong decrease in τ_{eff} from $\simeq 3$ to $\simeq 0.8$. Applying their $\Gamma_{\text{HeII}}(z)$ to the Nyx skewers we obtain a strongly evolving $\tau_{\text{eff}}(z)$ that agrees very well (maximum relative deviation 5%) with the prediction from the empirical IGM absorber model used by Puchwein et al. (2019). In addition, we use the Nyx skewers to predict the scatter of τ_{eff} on our adopted scale $\Delta z = 0.04$. A comparison to our τ_{eff} measurements in Figure 3 reveals that the redshift-dependent but spatially uniform $\Gamma_{\text{HeII}}(z)$ from Puchwein et al. (2019) significantly overpredicts the observed median τ_{eff} and underpredicts its scatter at $2.7 \lesssim z \lesssim 2.8$, suggesting that Γ_{HeII} is actually higher on average and spatially varying. Moreover, our ubiquitously low τ_{eff} at $z \simeq 2.9$ (see also W16) indicates that He II reionization finishes too late in the Puchwein et al. (2019) model.

In contrast, the redshift evolution of the He II effective optical depth predicted by the D17 fluctuating UV background model is in very good agreement with our measurements. At $z < 3$ both the median and the scatter in the observed τ_{eff} distribution are well reproduced. Applying the spatially fluctuating Γ_{HeII} from D17 to the realistic IGM density field in the Nyx simulation result in a consistent range in τ_{eff} on the considered scale $\Delta z = 0.04$. In the D17 model the tails of the τ_{eff} distribution are driven by the volume of space far away from and very close to quasars, corresponding to regions with low and high Γ_{HeII} , respectively. At $z > 3$ the model predicts a large scatter in τ_{eff} due to the decreasing space density of quasars and increasing spatial fluctuations in the mean free path to He II-ionizing photons. The lowest τ_{eff}

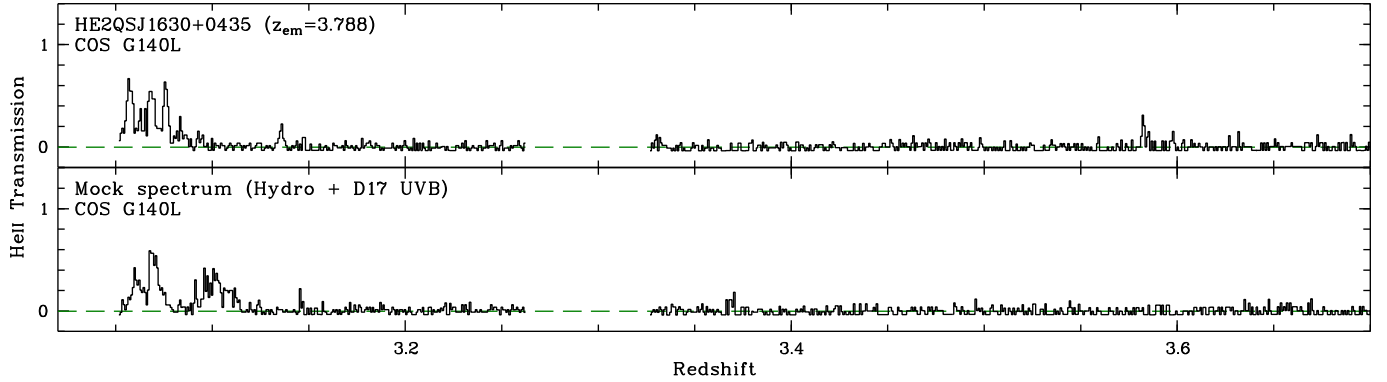


Figure 6. Comparison of an observed COS G140L He II transmission spectrum (top) and a mock spectrum (bottom). The mock spectrum was generated by applying a lightcone realization of the fluctuating He II-ionizing background from D17 to concatenated skewers from the Nyx hydrodynamical simulation at different redshifts, and simulating the observed continuum and noise characteristics.

values at these redshifts are produced by intersected isolated quasar proximity zones (Davies & Furlanetto 2014; D17). The rest of the volume may have substantially higher He II fractions, such that the assumption of photoionization equilibrium breaks down and a proper treatment of He II reionization becomes necessary. Because saturation in He II Ly α at $z > 3$ limits constraints on the He II fraction to a few percent at most (McQuinn 2009; Khrykin et al. 2016; Worseck et al. 2016), our data cannot discriminate between ongoing He II reionization and residual UV background fluctuations in a post-reionization IGM at $z > 3$. For a detailed statistical comparison, however, it is necessary to forward model the predicted $\tau_{\text{eff}}(z)$ distribution to account for data quality and sample size.

5.3. Generation of Realistic Mock COS Spectra

To produce realistic mock COS spectra from the rescaled Nyx skewers we took a forward-modeling approach similar to W16. In each $\Delta z = 0.04$ bin the contributing *HST/COS* He II sightlines have a somewhat different sensitivity to high τ_{eff} values due to their varying exposure time, continuum level, spectral dispersion, and time-dependent background conditions. First, the same number of skewers was drawn randomly from the set of 900 Nyx skewers for the considered Γ_{HeII} model and centered on the redshift bin. The Nyx skewers were convolved with the line spread functions of the actual *HST/COS* He II spectra, accounting for the different central wavelengths and COS LPs. From the initial $\Delta z = 0.08$ skewers only the central $\Delta z = 0.04$ part was kept to account for the wings of the COS G140L line spread function. With the specific parameters of the *HST/COS* spectra (quasar continuum, grating sensitivity, binning, pixel exposure time, background) the convolved Nyx skewers were converted to expected COS counts per pixel. Realistic COS counts were simulated by drawing from a Poisson distribution with a mean equal to the expected COS counts. For each spectrum a systematic background subtraction error across the $\Delta z = 0.04$ bin was incorporated by adding to the background a Gaussian random number with zero mean and standard deviation equal to the estimated background error for the considered spectral region. Then the Poisson counts

were converted to He II transmission with the modified background. Finally, τ_{eff} was evaluated in the mock COS spectra as described in Section 4.1. In particular, this ensured a proper treatment of the sightline-specific τ_{eff} sensitivity limits as in the observed spectra.

For each Γ_{HeII} model and $\Delta z = 0.04$ bin, the above procedure was repeated 2000 times to generate a statistical ensemble of subsample realizations. To illustrate its fidelity, we plot in Figure 6 the *HST/COS* He II transmission spectrum of HE2QS J1630+0435 and a mock spectrum using a lightcone skewer from the D17 fluctuating He II-ionizing background model. At $3.05 < z < 3.12$ the skewer intersects a He III zone with a peak value of $\Gamma_{\text{HeII}} \approx 6 \times 10^{-15} \text{ s}^{-1}$, giving rise to large-scale He II transmission that closely mimics the prominent He II transmission region toward HE2QS J1630+0435. Small-scale structure in the mock transmission region is impacted by Poisson noise, but still reflects variations in the density field drawn from the Nyx skewers. The generally strong He II absorption masks large-scale correlations and small discontinuities in the density field that arise from simply concatenating independent $\Delta z = 0.04$ Nyx skewers.

5.4. Statistical Comparison of Observed and Mock Data

In the mock spectra, the primary measure of interest is the τ_{eff} distribution that closely mimics the sensitivity limit of the *HST/COS* spectra. In the top panels of Figure 7 we compare the observed cumulative τ_{eff} distributions in the five $z < 3$ redshift ranges (Table 5) to the respective cumulative τ_{eff} distributions of mock data assuming several constant He II photoionization rates on a logarithmic grid. Due to sample variance, individual realizations of mock subsamples with n mock τ_{eff} values scatter around the distribution obtained from the total 2000 realizations. Nevertheless, the mock distributions can be clearly distinguished from another, allowing us to constrain Γ_{HeII} (see below). The mock distributions have characteristic shapes due to τ_{eff} sensitivity limits which occur more frequently at low Γ_{HeII} .

For a quantitative comparison of the observed and the mock data we use the Kolmogorov-Smirnov summary statis-

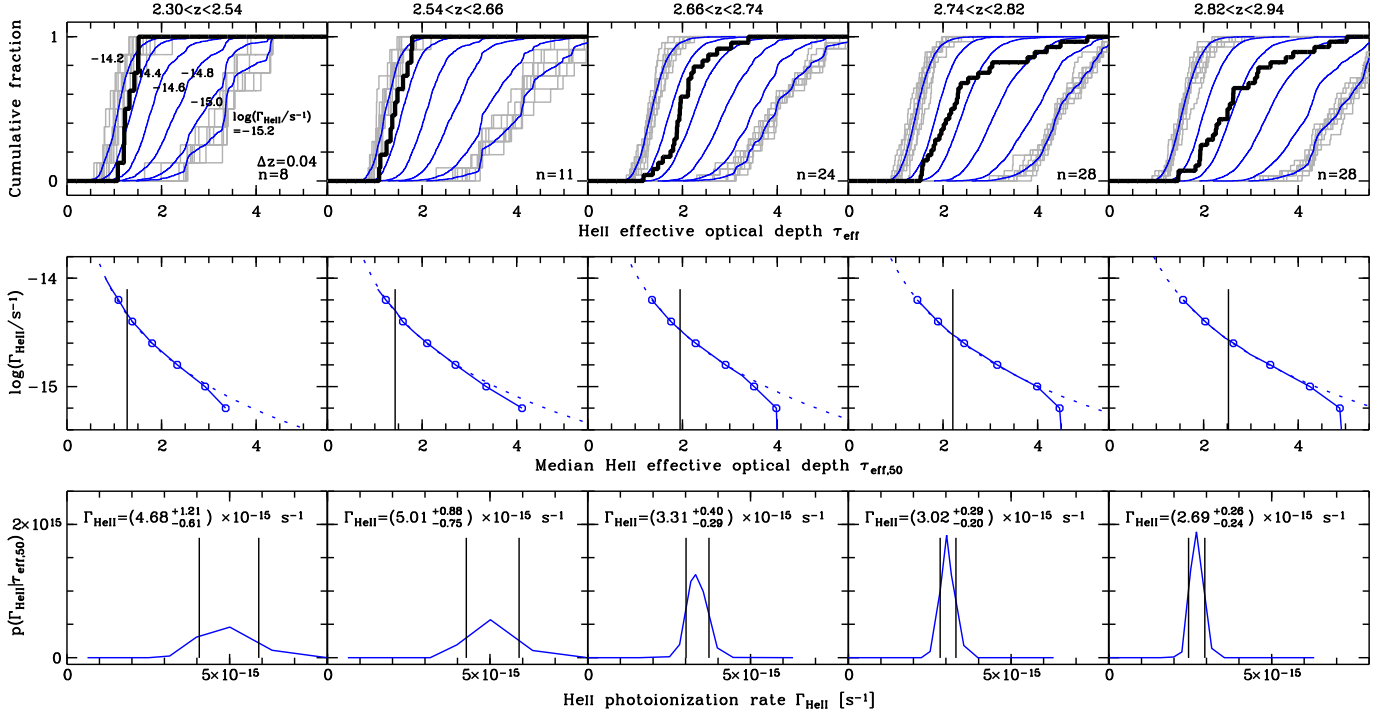


Figure 7. *Top:* Cumulative τ_{eff} distributions on a scale $\Delta z = 0.04$ for observed COS He II spectra (thick black, Table 5) and for realistic mock COS spectra from the Nyx hydrodynamical simulation for a uniform UV background assuming six different constant He II photoionization rates Γ_{HeII} (labeled) in five redshift ranges at $z < 3$ defined in Table 4. The blue curves show the merged samples of 2000 realizations of mock data samples with n values each, and sample variance is indicated for the minimum and maximum considered Γ_{HeII} by plotting 10 representative realizations (gray). *Middle:* Γ_{HeII} corresponding to the median τ_{eff} in the merged mock samples (solid curves). The values of the specific models in the top panel are indicated with circles. In noise-free simulated spectra the median τ_{eff} is well described by a power-law $\tau_{\text{eff},50} = a \Gamma_{\text{HeII}}^{-b}$ that varies with redshift (dotted curves). The measured $\tau_{\text{eff},50}$ from Table 4 is indicated by the vertical lines, yielding inferred values of Γ_{HeII} . *Bottom:* Normalized posterior of Γ_{HeII} given the measured $\tau_{\text{eff},50}$ in the considered redshift ranges. The 16th and the 84th percentile of the integral of the posterior (vertical lines) yield a 1σ confidence interval on Γ_{HeII} inferred from the middle panels (labeled).

tic

$$D = \max_k \left| F \left(\tau_{\text{eff}}^k \right) - H \left(\tau_{\text{eff}}^k | \Gamma_{\text{HeII}} \right) \right|, \quad (5)$$

where $F \left(\tau_{\text{eff}}^k \right)$ is the empirical cumulative distribution function to the k th highest out of n τ_{eff} values in the subsample (Table 5), and H is the hypothesized cumulative distribution function of τ_{eff} given Γ_{HeII} that is computed from the set of 2000 realizations. Computing the summary statistic for the individual mock subsamples we obtain an estimate of the distribution of D due to sample variance (i.e. the difference between the gray histograms and the blue curves in Figure 7), while the observed data yield a value D_{obs} . The fraction of mock realizations with $D > D_{\text{obs}}$ yields an estimate of the probability $P \left(> D_{\text{obs}} \right)$ that the model (i.e. a given constant Γ_{HeII}) is consistent with the data, with small values of this probability indicating inconsistency.

The spread in the model distributions in the top panels of Figure 7 reveals that each subsample is consistent with a narrow range in Γ_{HeII} . At $z < 2.66$ the data set is sparse, but only the model with $\Gamma_{\text{HeII}} = 10^{-14.4} \text{ s}^{-1}$ is consistent with the data ($P \left(> D_{\text{obs}} \right) = 0.205$ at $2.30 < z < 2.54$ and $P \left(> D_{\text{obs}} \right) = 0.250$ at $2.54 < z < 2.66$). We will give confidence intervals of Γ_{HeII} below. At $2.66 < z < 2.74$, the

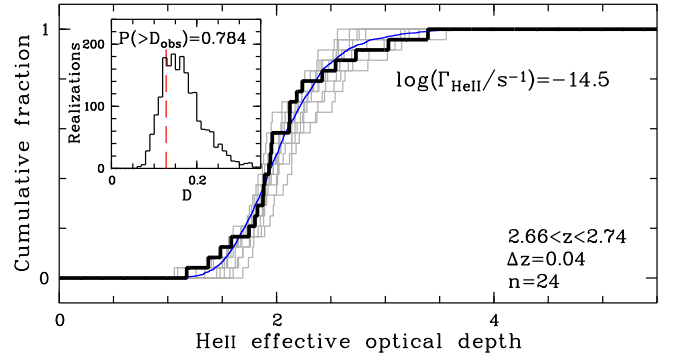


Figure 8. Observed cumulative τ_{eff} distribution on a scale $\Delta z = 0.04$ at $2.66 < z < 2.74$ (thick black) compared to mock distributions from the Nyx simulation with $\Gamma_{\text{HeII}} = 10^{-14.5} \text{ s}^{-1}$ (blue: all 2000 realizations with $n = 24$ values each, gray: 10 representative realizations to indicate sample variance). The inset shows the distribution of the maximum distance D between the cumulative τ_{eff} distributions of individual realizations and all mock data (Equation 5). The dashed line marks the value $D_{\text{obs}} = 0.1280$ of the actual data and all mock data. A high $P \left(> D_{\text{obs}} \right) = 0.784$ indicates that the model is consistent with the data.

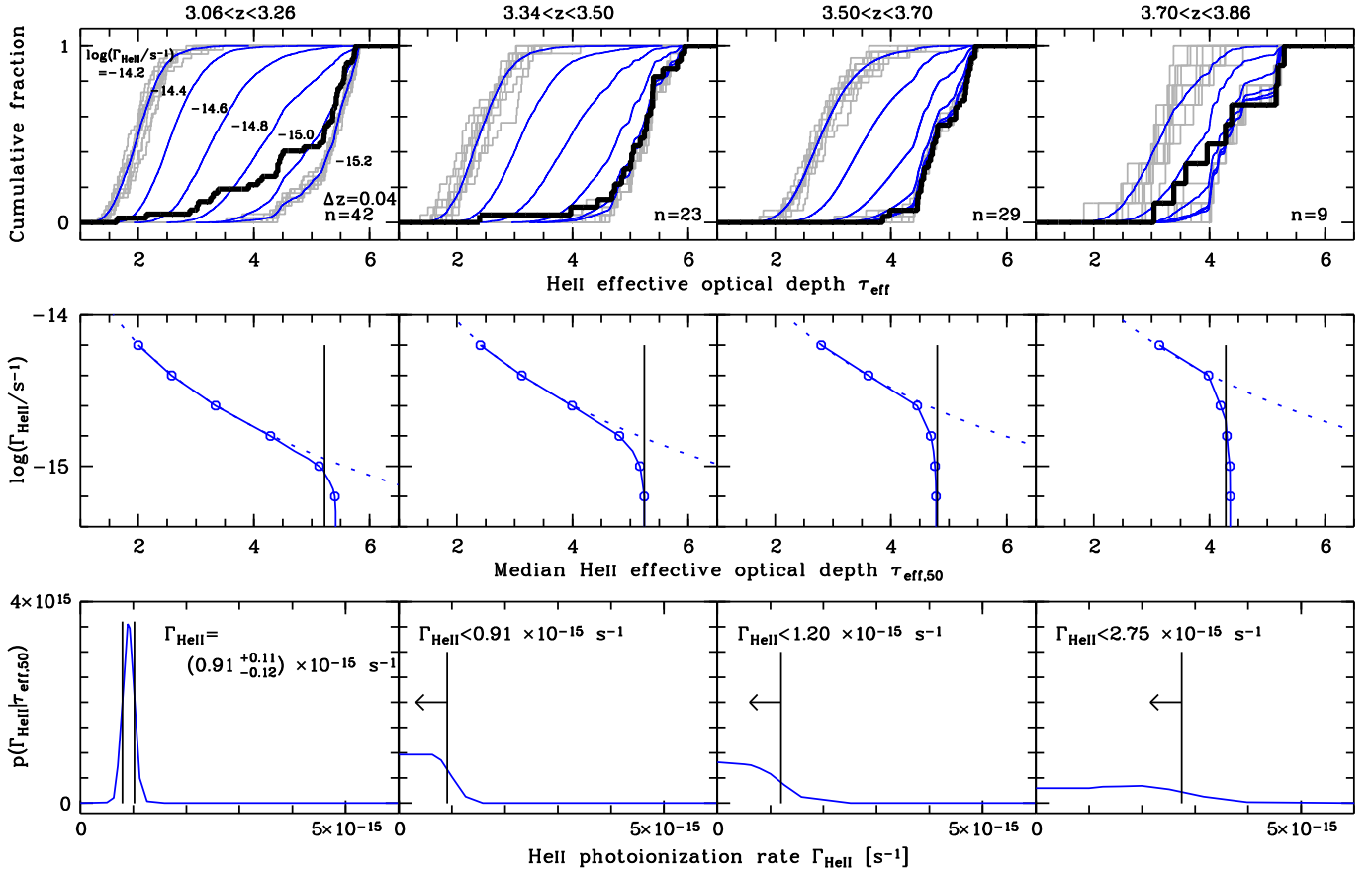


Figure 9. Similar to Figure 7, but showing the four subsamples at $z > 3$.

models with $\Gamma_{\text{HeII}} = 10^{-14.4} \text{ s}^{-1}$ and $\Gamma_{\text{HeII}} = 10^{-14.6} \text{ s}^{-1}$ are inconsistent with the data ($P(> D_{\text{obs}}) = 0.004$ and 0.007 , respectively), but bracket the observed τ_{eff} distribution. To investigate this further, we simulated the τ_{eff} distribution for $\Gamma_{\text{HeII}} = 10^{-14.5} \text{ s}^{-1}$, finding a very good match to the data ($P(> D_{\text{obs}}) = 0.784$), as illustrated in Figure 8. The agreement between the model and the data in Figure 8 indicates that the He II-ionizing background at $z \approx 2.7$ is quasi-uniform at an amplitude $\Gamma_{\text{HeII}} \approx 10^{-14.5} \text{ s}^{-1}$, and that the scatter in τ_{eff} is consistent with density fluctuations on the chosen scale $\Delta z = 0.04$ that are reproduced in the Nyx simulation.

At higher redshifts none of the uniform UV background models are consistent with the data. As shown in the top panels of Figure 7 the observed τ_{eff} distributions at $z > 2.74$ show a much larger spread than the mock distributions for any constant Γ_{HeII} . Consequently, also any spatially uniform but redshift-dependent He II-ionizing background (e.g. Faucher-Giguère et al. 2009; Haardt & Madau 2012; Puchwein et al. 2019) will not reproduce the observed τ_{eff} distribution at $z > 2.74$. Instead, the tail toward high τ_{eff} likely indicates fluctuations in the He II-ionizing background that are either due to the sparse source population (Davies & Furlanetto 2014; D17) or ongoing He II reionization (Worseck et al. 2011; W16).

Figure 9 shows the cumulative τ_{eff} distributions in the four $z > 3$ subsamples (Table 5). At $3.06 < z < 3.26$ the ob-

servations are still sensitive to a range in Γ_{HeII} , but uniform UV background models do not reproduce the large spread in the observed τ_{eff} distribution. The steep increase in the observed cumulative τ_{eff} distribution at $\tau_{\text{eff}} > 5$ is due to the very similar sensitivity limits of the contributing spectra. At $z > 3.3$ the frequent τ_{eff} sensitivity limits affect our constraints on Γ_{HeII} and possible UV background fluctuations. Nevertheless, based on the few low τ_{eff} measurements and the trend from lower redshifts, a non-uniform He II-ionizing background is favored. The apparent agreement of the data at $3.50 < z < 3.70$ with a uniform UV background with $\Gamma_{\text{HeII}} \lesssim 10^{-15} \text{ s}^{-1}$ is a mere coincidence due to the frequent sensitivity limits. For such low Γ_{HeII} values the τ_{eff} distribution is saturation-limited, so the apparent agreement just indicates that our model for noise and systematics is reasonable, rather than the existence of a uniform low-amplitude UV background.

5.5. The Median He II Photoionization Rate

Given the very good agreement of the data with a uniform UV background at $z \lesssim 2.7$ (Figure 8) and the sufficient dynamic range in Γ_{HeII} from our mock spectra, we investigated how to infer Γ_{HeII} as a function of redshift. We chose the median τ_{eff} as a representative value in each redshift range (Table 4), since it is well defined and robust to sample variance at $2.66 < z < 2.94$. The tails of the τ_{eff} distributions are

due to IGM density fluctuations and fluctuations in Γ_{HeII} , but these cannot be readily disentangled. As we will show below, the measured median τ_{eff} allows us to obtain an estimate of the characteristic Γ_{HeII} value of a mildly fluctuating UV background, whereas our summary statistic D is highly sensitive to the shape of the τ_{eff} distribution that is not reproduced by a uniform Γ_{HeII} model at $z > 2.74$.

The middle panels in Figures 7 and 9 show the relation between the median τ_{eff} and Γ_{HeII} from the Nyx simulation output. In noise-free simulated spectra the median τ_{eff} is well described by a power-law $\tau_{\text{eff},50} = a\Gamma_{\text{HeII}}^b$ with parameters a and b that slightly vary with redshift (dotted lines in Figures 7 and 9). At low Γ_{HeII} the realistic mock data depart from the power-law relation due to the characteristic sensitivity limit of the observed data. At $z < 3$ the measured $\tau_{\text{eff},50}$ is well below the sensitivity limit, such that Γ_{HeII} can be inferred. At $z > 3$, however, the measured $\tau_{\text{eff},50}$ is close to or at the sensitivity limit characterized by a sharp turnover of Γ_{HeII} as a function of $\tau_{\text{eff},50}$, implying a sensitivity limit to Γ_{HeII} at $z > 3.3$ (Figure 9).

To obtain a confidence interval for Γ_{HeII} we ran 2000–5000 mock sample realizations per input Γ_{HeII} value on a dense grid in Γ_{HeII} around the value implied by the data. On the mock sample realizations we performed Gaussian kernel density estimation to describe the likelihood $L(\tau_{\text{eff},50}|\Gamma_{\text{HeII}})$. Kernel widths and number of realizations were chosen to accurately reproduce multimodal distributions arising from slightly different sensitivity limits of the contributing spectra. According to Bayes’ Theorem the posterior probability distribution $p(\Gamma_{\text{HeII}}|\tau_{\text{eff},50})$ is related to the likelihood $L(\tau_{\text{eff},50}|\Gamma_{\text{HeII}})$ via

$$p(\Gamma_{\text{HeII}}|\tau_{\text{eff},50}) = \frac{L(\tau_{\text{eff},50}|\Gamma_{\text{HeII}})p(\Gamma_{\text{HeII}})}{p(\tau_{\text{eff},50})}, \quad (6)$$

with the prior probability distribution $p(\Gamma_{\text{HeII}})$ and the evidence $p(\tau_{\text{eff},50}) = \int L(\tau_{\text{eff},50}|\Gamma_{\text{HeII}})p(\Gamma_{\text{HeII}})d\Gamma_{\text{HeII}}$ that is the normalization of the posterior probability distribution. With the grid in Γ_{HeII} and the measured $\tau_{\text{eff},50}$ we constructed the posterior $p(\Gamma_{\text{HeII}}|\tau_{\text{eff},50})$, assuming a linear prior. While a logarithmic prior might be preferable to explore the range of Γ_{HeII} during He II reionization, such a prior is improper due to the saturation limit of the data at $z > 3.3$. Given our limited sensitivity to high τ_{eff} there would be an arbitrary large prior volume at low $\log \Gamma_{\text{HeII}}$, and even for a restricted range in $\log \Gamma_{\text{HeII}}$ the confidence intervals would depend on the lower and upper limit of Γ_{HeII} . For this reason we chose a linear prior, since $\Gamma_{\text{HeII}} = 0$ can be represented in a non-infinite parameter volume, but we caution that our limits on Γ_{HeII} obtained from τ_{eff} sensitivity limits are sensitive to this choice.

The resulting posterior distributions are shown in the bottom panels of Figures 7 and 9. Equal-tailed 1σ confidence intervals were obtained by integrating the normalized posteriors to 0.16 and 0.84, respectively. At $z < 3.3$ the posteriors are strongly peaked and their widths are primarily given by sample size. At higher redshifts the posteriors

Table 6. Median He II photoionization rate Γ_{HeII} and corresponding median He II fraction x_{HeII} in redshift ranges Δz

Δz	$\Gamma_{\text{HeII}} \left(10^{-15} \text{ s}^{-1} \right)$	$x_{\text{HeII}} (\%)$
2.30–2.54	$4.68^{+1.21}_{-0.61}$	$0.29^{+0.04}_{-0.06}$
2.54–2.66	$5.01^{+0.88}_{-0.75}$	$0.32^{+0.05}_{-0.05}$
2.66–2.74	$3.31^{+0.40}_{-0.29}$	$0.52^{+0.05}_{-0.06}$
2.74–2.82	$3.02^{+0.29}_{-0.20}$	$0.61^{+0.04}_{-0.05}$
2.82–2.94	$2.69^{+0.26}_{-0.24}$	$0.73^{+0.07}_{-0.06}$
3.06–3.26	$0.91^{+0.11}_{-0.12}$	$2.54^{+0.26}_{-0.37}$
3.34–3.50	< 0.91	> 3.15
3.50–3.70	< 1.20	> 2.71
3.70–3.86	< 2.75	> 1.47

are non-zero at $\Gamma_{\text{HeII}} = 0$, indicating the sensitivity limit of the data. For each redshift range where the posterior at $\Gamma_{\text{HeII}} = 0$ is at or close to its peak value (in practice we choose $p(\Gamma_{\text{HeII}} = 0|\tau_{\text{eff},50}) > 10^{14}$ in Figure 9) we obtained a 1σ upper limit on Γ_{HeII} by integrating the posterior to 0.84. Our inferred values and limits of Γ_{HeII} are listed in Table 6.

The above inferences assume a uniform Γ_{HeII} across the redshift ranges of the subsamples. Since uniform models fail to reproduce the data at $z > 2.74$ we may question the meaning of the inferred Γ_{HeII} values at these redshifts. We explored this by producing mock spectra for several Γ_{HeII} distributions in the representative redshift range $2.74 < z < 2.82$. For each of the 28 $\Delta z = 0.04$ bins from 15 contributing COS He II sightlines we randomly drew a Γ_{HeII} value from the chosen distribution, assumed it to be constant across the $\Delta z = 0.04$ bin, and generated a mock spectrum as before. From 2000 mock data sets we obtained the distribution of $\tau_{\text{eff},50}$ and the inferred Γ_{HeII} . Figure 10 shows the results for a uniform and a lognormal Γ_{HeII} distribution. For a uniform Γ_{HeII} the median τ_{eff} recovers the input value, with the 1σ scatter dominated by sample variance. For an underlying lognormal Γ_{HeII} distribution the median τ_{eff} approximately yields the median Γ_{HeII} . The variance in the inferred Γ_{HeII} increases due to the sampling from the Γ_{HeII} distribution. Tests with several other skewed or bimodal distributions gave similar results close to the median of the input distribution. While we cannot rigorously show that this holds in general, we note that the statistical error inferred from the output Γ_{HeII} distribution is much larger than systematic deviations between the assumed and the revealed median Γ_{HeII} even for a uniform Γ_{HeII} . Therefore we conclude that our measurements approximately recover the median Γ_{HeII} of a fluctuating He II-ionizing background.

5.6. Fluctuations in the He II-Ionizing Background

Analogously to the uniform UV background models presented in Section 5.4, we show in Figure 11 the comparison of the observed cumulative τ_{eff} distributions to the respective mock τ_{eff} distributions assuming the fluctuating UV background model from D17. We reiterate that we have not tuned the D17 model parameters (quasar luminosity func-

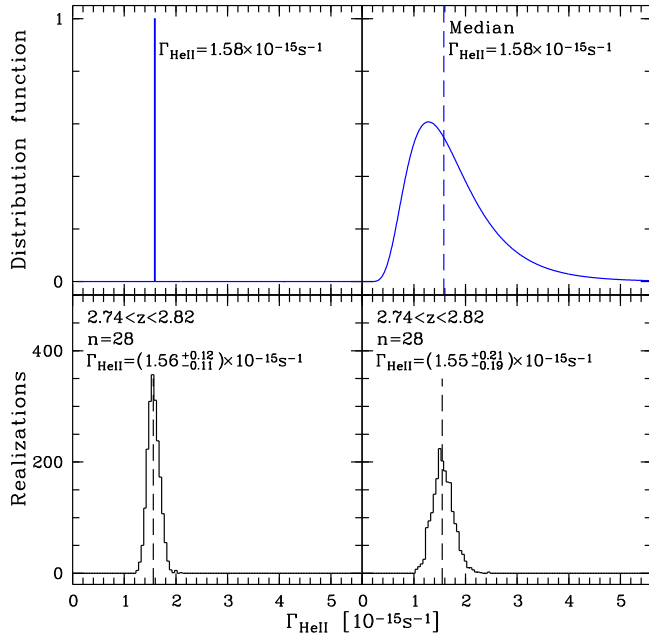


Figure 10. *Top:* Two input distributions of Γ_{HeII} (left: uniform, right: lognormal but constant on scales $\Delta z = 0.04$) with indicated median value (dashed and labeled). *Bottom:* Distributions of Γ_{HeII} values inferred from 2000 mock data sets at $2.74 < z < 2.82$. Dashed lines mark the median values. The median τ_{eff} approximately recovers the median value of the input Γ_{HeII} distribution.

tion, quasar spectral energy distribution, quasar lightcurve and opening angle, IGM absorption) to fit our τ_{eff} distributions. Further exploration of the partially degenerate parameter space constrained by recent observational data and inferences (e.g. Inoue et al. 2014; Khaire 2017; Schmidt et al. 2018; Khrykin et al. 2019; Kulkarni et al. 2018b) is left for future work.

High values of $P(> D_{\text{obs}})$ indicate that the model is in remarkable agreement with the data in most of the considered redshift ranges. In particular, in contrast to the uniform UV background models, the D17 model reproduces the observed skewed τ_{eff} distributions at $z > 2.74$ that are due to the combined effect of fluctuations in the density field and the UV background.

Minor mismatches of the data and the model occur at the lowest and the highest redshifts ($2.66 < z < 2.74$ and $3.70 < z < 3.86$), which may be due to the particular choice of model parameters (i.e. quasar and IGM absorber properties) or remaining cosmic variance due to the small number of bright $z > 3$ quasars in the $(500 \text{ cMpc})^3$ simulation volume (D17). Since the τ_{eff} distribution at $2.66 < z < 2.74$ is consistent with a uniform UV background (Figure 8) we tested whether the minor inconsistency at $2.66 < z < 2.74$ is due to diminishing UV background fluctuations (the D17 model predicts variations by a factor ≈ 1.5 around the median Γ_{HeII} at $z = 2.7$). Comparing mock samples generated with a uniform UV background to mock samples assuming the D17 fluctuating UV background, we found that a narrow range of

constant Γ_{HeII} values is consistent with the fluctuating model. We conclude that at $z \approx 2.7$ our data cannot distinguish between a uniform UV background and a mildly fluctuating one, and that the minor discrepancy in the τ_{eff} distribution can be resolved by an insignificant -0.05 dex adjustment of the median Γ_{HeII} in the D17 model at $z \approx 2.7$.

At $z > 3$ the D17 model reproduces the tail toward low τ_{eff} values, indicating that these are likely due to intersected proximity zones of quasars. The model predicts a somewhat stronger tail than observed, which may require either adjustments in the model parameters or proper modeling of the He II reionization process that becomes relevant at $z > 3$ (Davies & Furlanetto 2014; D17). The overall good agreement indicates that the D17 model successfully captures the percolation of He III zones around quasars at $z \gtrsim 3$. For saturated regions in our He II spectra, however, we cannot tell whether they correspond to downward UV background fluctuations in a post-reionization IGM ($\Gamma_{\text{HeII}} \lesssim 10^{-15} \text{ s}^{-1}$) or to not yet reionized He II patches ($\Gamma_{\text{HeII}} \rightarrow 0$). The observed excess toward low τ_{eff} values at $z > 3.7$ that is inconsistent with the model despite the small sample ($P(> D_{\text{obs}}) = 0.014$) may be due to large-scale correlations in the radiation field in the peculiar SDSS J1319+5202 sightline (Section 4.2) or due to a particularly small number of $z \sim 3.8$ quasars in the $(500 \text{ cMpc})^3$ simulation volume. Analysis of a second $(500 \text{ cMpc})^3$ volume yields similar results at $z > 3$, indicating that the predicted τ_{eff} distribution is not strongly affected by cosmic variance given our sample size and limited τ_{eff} sensitivity.

6. DISCUSSION

6.1. Redshift Evolution of the He II-Ionizing Background

In Figure 12 we compare the redshift evolution of Γ_{HeII} inferred from our τ_{eff} sample to several published estimates and models. We reiterate that our values approximately correspond to the median values for a range of plausible Γ_{HeII} distributions (Figure 10), but our τ_{eff} measurements cannot well constrain the Γ_{HeII} distribution or the spatial scale of Γ_{HeII} fluctuations. The He II photoionization rate drops by a factor of ≈ 5 between $z \approx 2.6$ and $z \approx 3.1$. The decrease likely continues to $z > 3.3$ where our constraints on Γ_{HeII} are limited by saturation, instrument sensitivity and sample size.

At $z \approx 3.1$ our Γ_{HeII} value is consistent with the estimate $\Gamma_{\text{HeII}} = 10^{-14.9 \pm 0.2} \text{ s}^{-1}$ by Khrykin et al. (2016) that was based on a rough comparison of a subset of our τ_{eff} data to a $25 h^{-1} \text{ cMpc}$ smoothed particle hydrodynamics simulation without forward-modeling to the actual data quality. Khaire (2017) matched the median τ_{eff} values from W16 to predictions for an optically thin IGM in photoionization equilibrium by applying a model for the He II-to-H I number density ratio $n_{\text{HeII}}/n_{\text{HI}}$ to the H I column density distribution $f(N_{\text{HI}}, z)$ which yields Γ_{HeII} for an assumed value of Γ_{HI} . The estimates critically depend on the assumed $f(N_{\text{HI}}, z)$ and the minimum N_{HI} for Ly α forest lines, so the systematic offset between our values and the ones by Khaire (2017) is not

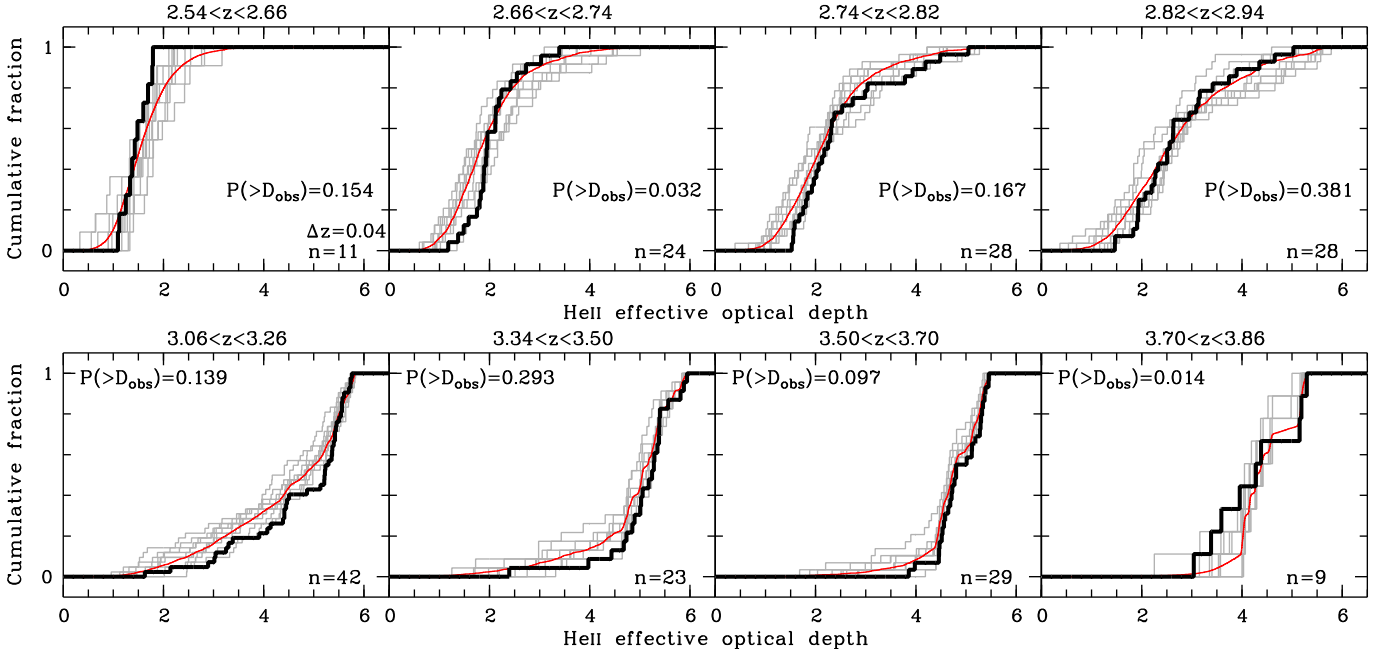


Figure 11. Cumulative τ_{eff} distributions on a scale $\Delta z = 0.04$ for observed COS He II spectra (thick black, Table 5) and for realistic mock COS spectra from the Nyx hydrodynamical simulation applying the fluctuating UV background model from Davies et al. (2017) in eight of the redshift ranges defined in Table 4. The red curves show the merged samples of 2000 realizations of mock data samples with n values each, and sample variance is indicated by plotting 10 representative realizations (gray). For each redshift range we list the estimated probability $P(> D_{\text{obs}})$ that the model is consistent with the data (Section 5.4).

surprising⁵. McQuinn & Worseck (2014) analyzed the co-eval H I and He II Ly α absorption in two post-reionization ($2.4 < z < 2.7$) He II sightlines calibrated to a smoothed particle hydrodynamics simulation, finding small (factor < 2) variations of the number density ratio $n_{\text{HeII}}/n_{\text{HI}}$ around a value of ≈ 100 on scales of a few cMpc. With $\Gamma_{\text{HI}} = 0.5\text{--}1 \times 10^{-12} \text{ s}^{-1}$ (Faucher-Giguère et al. 2008; Becker & Bolton 2013) they estimated $\Gamma_{\text{HeII}} = 2\text{--}4 \times 10^{-15} \text{ s}^{-1}$, with the true value being probably closer to the upper end of this range (see Becker & Bolton 2013 for a discussion on Γ_{HI}). The remaining small differences to our Γ_{HeII} values are probably caused by the different thermal history employed in the simulation used by McQuinn & Worseck (2014).

Figure 12 also shows model predictions for $\Gamma_{\text{HeII}}(z)$. The recent uniform UV background synthesis model by Puchwein et al. (2019) is in broad agreement with our inferred Γ_{HeII} values at $z \lesssim 2.7$. Since our inferences assume photoionization equilibrium, we plot their equivalent-equilibrium $\Gamma_{\text{HeII}}(z)$. At $z > 2.7$ the Puchwein et al. (2019) He II photoionization rate drops much more rapidly than our measurements. This is primarily due to rapid evolution in the He III volume filling factor during He II reionization that completes at $z \approx 2.8$ in the Puchwein et al. (2019) model for their particular choice of quasar emissivity and IGM clump-

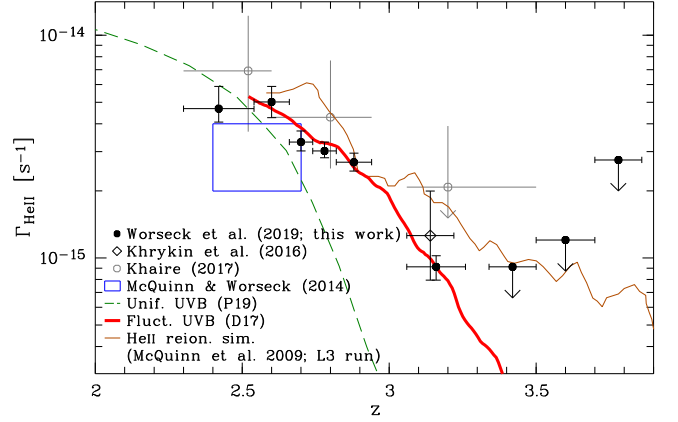


Figure 12. He II photoionization rate as a function of redshift. Filled circles show the Γ_{HeII} values inferred from the median τ_{eff} in the indicated redshift ranges (Table 6). Error bars are 1σ derived from the posterior of Γ_{HeII} given the measured median τ_{eff} , and arrows indicate 1σ upper limits. We also show previous estimates based on subsets of our data (Khrykin et al. 2016; Khaire 2017) or inferred from the number density ratio $n_{\text{HeII}}/n_{\text{HI}}$ (McQuinn & Worseck 2014). Lines show predictions based on a 1D uniform UV background synthesis model (Puchwein et al. 2019), 3D semianalytic calculations with a fluctuating UV background (Davies et al. 2017), and a 3D numerical radiative transfer simulation of He II reionization (McQuinn et al. 2009).

⁵ Khaire (2017) incorrectly estimated the error on the median τ_{eff} from the distribution of errors of individual τ_{eff} measurements. In Figure 12 we show his overestimated propagated errors for Γ_{HeII} , noting that there are additional systematic uncertainties due to the assumed $f(N_{\text{HI}}, z)$.

ing factor. During reionization the Puchwein et al. (2019) Γ_{HeII} represents an average over the inhomogeneously ion-

ized Universe captured by the He III volume filling factor. Since our values incorporate fully and partially ionized regions characterized by low and high τ_{eff} , respectively, they are comparable to Puchwein et al. (2019) if the Γ_{HeII} distribution is not highly skewed or bimodal. The observed shallow redshift evolution of the He II effective optical depth (Figure 3) and the inferred He II photoionization rate both indicate that He II reionization proceeded more gradually or ended earlier than predicted by Puchwein et al. (2019). Indeed, the He III volume filling factor is expected to evolve gradually at the end of reionization when the opacity to ionizing photons is dominated by Lyman limit systems instead of the diffuse IGM (e.g. Furlanetto & Oh 2005; Furlanetto & Oh 2008a; Bolton et al. 2009a; Madau 2017). Puchwein et al. (2019) did not model He II Lyman limit systems explicitly, which likely resolves the discrepancy to our median τ_{eff} values and the inferred Γ_{HeII} at $z > 2.7$.

The median $\Gamma_{\text{HeII}}(z)$ from the D17 fluctuating UV background model (thick red line in Figure 12) matches our inferred values very closely at $z < 3.3$ where our data set has sufficient sensitivity. This directly follows from the good agreement of the τ_{eff} distributions (Figure 11). The mean Γ_{HeII} from D17 (not shown) is higher than the median at all redshifts, in particular at $z > 3$, since it is dominated by ionized regions. D17 predict a strong redshift evolution of the median Γ_{HeII} due to the evolving quasar number density and the fluctuating mean free path in the post-reionization IGM.

Finally, the brown curve shows the volume-averaged $\Gamma_{\text{HeII}}(z)$ from a numerical simulation of He II reionization (McQuinn et al. 2009). Their L3 simulation, which includes a filtering prescription for low-column density systems, broadly reproduces the observed scatter in τ_{eff} at $2.7 \lesssim z \lesssim 3$ (W16). At $z > 3$ their volume-averaged Γ_{HeII} is dominated by He III regions, and the jaggedness of the curve is due to variance in the number of active quasars captured in the $(186 \text{ Mpc})^3$ simulation volume. Accounting for these differences and uncertainties, our inferred Γ_{HeII} values agree quite well with the McQuinn et al. (2009) radiative transfer simulation.

6.2. The Median He II Fraction

By combining our measurements of the median Γ_{HeII} with the Nyx simulation skewers, we can estimate the median fraction of He II, x_{HeII} , in the IGM, which we list in Table 6. While the median IGM has been fully reionized with $x_{\text{HeII}} < 1\%$ at $z < 3$, at $z > 3$ the median IGM has a substantial residual He II fraction of $x_{\text{HeII}} \gtrsim 2.5\%$, indicating that we are probing the tail end of the helium reionization process. A caveat here is that we are mainly sensitive to Γ_{HeII} and hence x_{HeII} in ionized regions, and that for highly bimodal distributions our estimate of the median value is strongly impacted by the limited sample size. As such, it is not yet clear how to relate our x_{HeII} value to the He III volume filling factor used in simple estimates of the He II reionization history (e.g. Haardt & Madau 2012; Madau 2017; Puchwein et al. 2019).

6.3. Uncertainties

In addition to the statistical errors computed in Section 5.5 our inferred Γ_{HeII} values may be affected by systematic uncertainties, primarily due to our approximation to use optically thin simulations to represent the immediate post-reionization IGM with potentially large variations in Γ_{HeII} and residual patches of He II. On the other hand, it is fair to assume photoionization equilibrium that allows a simple rescaling of optical depths in these simulations, since our inferred $\Gamma_{\text{HeII}} \gtrsim 10^{-15} \text{ s}^{-1}$ corresponds to an equilibration timescale $t_{\text{eq}} \approx \Gamma_{\text{HeII}}^{-1} \lesssim 3 \times 10^7$ years, which is short compared to any cosmological effect (McQuinn 2009; Khrykin et al. 2016).

A further systematic uncertainty stems from the specific thermal history assumed in the Nyx simulation, which depends on the amount of heat injected into the IGM during He II reionization. We estimate the magnitude of this effect by imposing two different IGM thermal states onto the Nyx skewers which bracket the $\sim 1\sigma$ range of the measurements by Walther et al. (2018) at $z = 3$: $(T_0, \gamma) = (10700 \text{ K}, 1.80)$ and $(15000 \text{ K}, 1.36)$, where the IGM temperature-density relation is defined to be a power law $T(\rho) = T_0 (\rho/\bar{\rho})^{\gamma-1}$ and $\bar{\rho}$ is the mean density of the Universe (Walther et al. 2019). Due to the temperature dependence of the He II recombination rate, these two thermal states require more or less photoionization by the UV background to match the same τ_{eff} . Compared to our fiducial simulation, the relatively cold and hot models (at mean density) would shift our inferred Γ_{HeII} values by approximately $+0.1$ and -0.2 dex, respectively. By comparison, the modest τ_{eff} convergence issues of our fiducial Nyx simulation result in a modest bias of our inferred Γ_{HeII} values by $+10\%$ (Appendix B).

A final caveat is that our statistical errors on Γ_{HeII} are possibly underestimated, because our inference just includes the variance in τ_{eff} due to density fluctuations and data quality, but not the variance of a fluctuating UV background. However, this is relevant when the UV background fluctuations are largest and occur on large scales, i.e. at $z > 3.3$ where we just obtain upper limits on Γ_{HeII} due to the sensitivity limit of our data. As our upper limits on Γ_{HeII} also depend on the assumed prior, we estimate that mild UV background fluctuations do not significantly increase our statistical errors.

7. SUMMARY AND CONCLUSIONS

We have conducted a systematic survey to characterize the ionization state of intergalactic helium at $2.3 < z < 3.8$ with *HST* He II Ly α absorption spectra. Building on earlier results (W16), we have analyzed *HST*/COS spectra of eight additional He II-transparent $z_{\text{em}} > 3$ quasars, six of which had been discovered in our dedicated survey for FUV-bright high-redshift quasars (dubbed HE2QS, Figure 1). These spectra increase the redshift pathlength sensitive to high He II effective optical depths $\tau_{\text{eff}} \sim 5$ by more than a factor of two at $3 < z < 3.5$, and provide the first statistically meaningful sample of six He II sightlines at $z > 3.5$. Adding archival higher-quality high-resolution spectra of four known He II-transparent quasars, we have constructed a total sample of 25 science-grade ($S/N \gtrsim 3$) *HST* He II Ly α absorption spectra,

available from our survey data repository ⁶. Our main results can be summarized as follows:

1. At $z > 3.5$ He II Ly α absorption is predominantly saturated with some isolated narrow ($\Delta v < 650 \text{ km s}^{-1}$) transmission spikes, most of which are unresolved and/or impacted by Poisson noise in our *HST*/COS G140L spectra (Figure 5). At $z < 3.5$ these features become more numerous and broader (Figure 4), but the He II Ly α absorption is still patchy at $2.7 < z < 3.3$ with significant sightline-to-sightline variance.
2. The He II effective optical depth on a scale $\Delta z = 0.04$ ($\approx 40 \text{ cMpc}$ at $z = 3$) increases from $\tau_{\text{eff}} \approx 2$ at $z = 2.7$ to a sensitivity limit $\tau_{\text{eff}} \gtrsim 5$ at $z > 3$, but with significant sightline-to-sightline variance at $z > 2.7$ that increases with redshift (Figure 3). At $z > 3$ regions with $\tau_{\text{eff}} < 5$ gradually disappear as a result of the diminishing number and significance of He II transmission spikes. At $z \approx 3.4$ our larger sample yields a lower fraction of statistically significant $\tau_{\text{eff}} \lesssim 5$ values (26.1%) than in W16 (50%), bringing the data into better agreement with numerical models of the fluctuating He II-ionizing radiation field at the tail end of He II reionization (Compostella et al. 2014; D17). Still, 6/38 $\Delta z = 0.04$ regions at $z > 3.5$ show statistically significant He II transmission.
3. We have compared our τ_{eff} measurements to predictions for a range of UV background models applied to outputs of a large ($100h^{-1} \text{ cMpc}$) high-resolution ($25h^{-1} \text{ ckpc}$) hydrodynamical simulation, forward-modeling variations in data quality and sample size. At $z > 2.74$ the observed variance in τ_{eff} cannot be reproduced by a spatially uniform redshift-dependent He II-ionizing background (Figure 7), strictly confining the applicability of common UV background synthesis models to $z < 2.74$ (e.g. Faucher-Giguère et al. 2009; Haardt & Madau 2012; Puchwein et al. 2019). Instead, the observed τ_{eff} distributions closely agree with predictions of the D17 fluctuating post-reionization UV background that is due to the varying quasar number density and the mean free path to He II-ionizing photons. This suggests an extended overlap epoch of He III zones around quasars at $2.7 \lesssim z \lesssim 3.3$ that is captured by the D17 model without deliberately tuning its parameters. However, at $z > 3.3$ we cannot distinguish between this scenario and ongoing He II reionization due to limited sensitivity to $\tau_{\text{eff}} \sim 5$ and model assumptions (Davies & Furlanetto 2014; D17).
4. We have developed a method to infer the characteristic He II photoionization rate by matching the median τ_{eff} of observed and mock data, respectively. Tests with mock data confirmed that our procedure approximately

recovers the median value of a Γ_{HeII} distribution with sightline-to-sightline variance but spatial coherence on the adopted scale $\Delta z = 0.04$. The inferred Γ_{HeII} decreases by a factor ≈ 5 between $z \approx 2.6$ and $z \approx 3.1$ (Figure 12), in very good agreement with the median $\Gamma_{\text{HeII}}(z)$ by D17. At $3.06 < z < 3.26$ our inferred $\Gamma_{\text{HeII}} = [9.1_{-1.2}^{+1.1} (\text{stat.})_{-3.4}^{+2.4} (\text{sys.})] \times 10^{-16} \text{ s}^{-1}$ translates to a median He II fraction $x_{\text{HeII}} \approx 0.025$, confirming that our sample of He II sightlines probes the tail end of He II reionization that is well approximated by the D17 fluctuating UV background model. At $z > 3.3$ our constraints are limited by saturation in He II Ly α due to IGM density evolution, decreasing instrument sensitivity, and a small sample size.

In summary, our sample of He II sightlines probes the extended end phase of He II reionization and the build-up of the He II-ionizing background with gradually diminishing fluctuations, in good agreement with recent models (Compostella et al. 2014; D17). At $z > 3$ the observed τ_{eff} distributions are consistent with models of He II reionization primarily driven by the observed quasar population at $z > 4$ (Compostella et al. 2014). At face value, our six $\tau_{\text{eff}} \lesssim 4$ values at $z > 3.5$ indicate mild tension with these models, which may be due to the few specific quasar models run on limited simulation volumes (e.g. D’Aloisio et al. 2017). Future progress requires large-volume He II reionization simulations with accurate radiative transfer (see La Plante et al. 2017 for a recent effort) but also more and higher-quality data. Our forthcoming *HST* program (PID 15356, PI Worseck) aims at resolving the He II Ly α absorption toward the two UV-brightest $z > 3.5$ He II-transmitting quasars discovered in our dedicated survey, to verify and resolve isolated narrow He II transmission spikes.

In the near future, optical slitless prism spectroscopy currently obtained by the *Gaia* satellite will provide a complete census of bright quasars on the full sky (e.g. Proft & Wambsganss 2015) that does not exhibit the specific bias against UV-bright $z_{\text{em}} > 2.7$ quasars in optical color-selected samples (Worseck & Prochaska 2011). Correlation of the *Gaia* quasar catalog to *GALEX* photometry will reveal further likely He II-transparent quasars to complete *HST*’s legacy on He II absorption spectroscopy. The physical interpretation of these data will require dedicated efforts to run large-volume radiative transfer simulations of He II reionization that use updated quasar luminosity functions (Kulkarni et al. 2018b) and the latest constraints on the distribution of quasar lifetimes (Eilers et al. 2017; Schmidt et al. 2018; Khrykin et al. 2019). These simulations will also make detailed predictions for the early stages of He II reionization at $z > 4$ that may be studied with sensitive He II absorption spectroscopy obtained with a next-generation large-aperture UV space telescope.

We thank Zarija Lukić for providing the Nyx simulation, Jose Oñorbe for help with the convergence test simulations, and Jo Bovy for adapting his algorithm to specifically select FUV-bright quasar candidates. We thank the referee for their helpful and constructive report.

⁶ <https://archive.stsci.edu/prepds/hers/>

Support for Programs GO 13013 and GO 13875 was provided by NASA through a grant from the Space Telescope Science Institute, which is operated by the Association of Universities for Research in Astronomy, Inc., under NASA contract NAS5-26555. G.W. has been partially supported by the Deutsches Zentrum für Luft- und Raumfahrt (DLR) through grant numbers 50 OR 1317 and 50 OR 1512. F.B.D. has been partially supported by NASA through grant number HST-AR-15014 from the Space Telescope Science Institute.

This work is based on observations collected at the Centro Astronómico Hispano Alemán (CAHA) at Calar Alto, operated jointly by the Max-Planck-Institut für Astronomie and the Instituto de Astrofísica de Andalucía (CSIC). It also uses data obtained from Lick Observatory, owned and operated by the University of California.

Funding for SDSS-III has been provided by the Alfred P. Sloan Foundation, the Participating Institutions, the National Science Foundation, and the U.S. Department of Energy Office of Science. The SDSS-III web site is <http://www.sdss3.org/>. SDSS-III is managed by the Astrophysical Research Consortium for the Participating Institutions of the SDSS-III Collaboration including the University of Arizona, the Brazilian Participation Group, Brookhaven National Laboratory, Carnegie Mellon University, University of Florida, the French Participation Group, the German Participation Group, Harvard University, the Instituto de Astrofísica de Canarias, the Michigan State/Notre Dame/JINA Participation Group, Johns Hopkins University, Lawrence Berkeley National Laboratory, Max Planck Institute for Astrophysics, Max Planck Institute for Extraterrestrial Physics, New Mexico State University, New York University, Ohio State University, Pennsylvania State University, University of Portsmouth, Prince-

ton University, the Spanish Participation Group, University of Tokyo, University of Utah, Vanderbilt University, University of Virginia, University of Washington, and Yale University.

The Pan-STARRS1 Surveys (PS1) and the PS1 public science archive have been made possible through contributions by the Institute for Astronomy, the University of Hawaii, the Pan-STARRS Project Office, the Max-Planck Society and its participating institutes (the Max Planck Institute for Astronomy, Heidelberg and the Max Planck Institute for Extraterrestrial Physics, Garching), The Johns Hopkins University, Durham University, the University of Edinburgh, the Queen's University Belfast, the Harvard-Smithsonian Center for Astrophysics, the Las Cumbres Observatory Global Telescope Network Incorporated, the National Central University of Taiwan, the Space Telescope Science Institute, the National Aeronautics and Space Administration under Grant No. NNX08AR22G issued through the Planetary Science Division of the NASA Science Mission Directorate, the National Science Foundation Grant No. AST-1238877, the University of Maryland, Eotvos Lorand University (ELTE), the Los Alamos National Laboratory, and the Gordon and Betty Moore Foundation.

This publication makes use of data products from the Wide-field Infrared Survey Explorer, which is a joint project of the University of California, Los Angeles, and the Jet Propulsion Laboratory/California Institute of Technology, funded by the National Aeronautics and Space Administration.

Facilities: HST (STIS, COS), CAO:2.2m (Calar Alto Faint Object Spectrograph), Shane (Kast Double Spectrograph), GALEX, PS1, Sloan, WISE

REFERENCES

- Aihara, H., Allende Prieto, C., An, D., et al. 2011, *ApJS*, 193, 29, doi: [10.1088/0067-0049/193/2/29](https://doi.org/10.1088/0067-0049/193/2/29)
- Almgren, A. S., Bell, J. B., Lijewski, M. J., Lukić, Z., & Van Andel, E. 2013, *ApJ*, 765, 39, doi: [10.1088/0004-637X/765/1/39](https://doi.org/10.1088/0004-637X/765/1/39)
- Anderson, S. F., Hogan, C. J., Williams, B. F., & Carswell, R. F. 1999, *AJ*, 117, 56
- Bahcall, J. N. 1979, in *NASA Conference Publication*, Vol. 2111, *Scientific Research with the Space Telescope: IAU Colloquium No. 54*, ed. M. S. Longair & J. W. Warner, 215–240
- Becker, G. D., & Bolton, J. S. 2013, *MNRAS*, 436, 1023
- Becker, G. D., Bolton, J. S., Haehnelt, M. G., & Sargent, W. L. W. 2011, *MNRAS*, 410, 1096
- Becker, G. D., Bolton, J. S., Madau, P., et al. 2015, *MNRAS*, 447, 3402, doi: [10.1093/mnras/stu2646](https://doi.org/10.1093/mnras/stu2646)
- Becker, G. D., Davies, F. B., Furlanetto, S. R., et al. 2018, *ApJ*, 863, 92, doi: [10.3847/1538-4357/aacc73](https://doi.org/10.3847/1538-4357/aacc73)
- Boera, E., Murphy, M. T., Becker, G. D., & Bolton, J. S. 2014, *MNRAS*, 441, 1916, doi: [10.1093/mnras/stu660](https://doi.org/10.1093/mnras/stu660)
- Bolton, J. S., & Becker, G. 2009, *MNRAS*, 398, L26
- Bolton, J. S., Becker, G. D., Haehnelt, M. G., & Viel, M. 2014, *MNRAS*, 438, 2499, doi: [10.1093/mnras/stt2374](https://doi.org/10.1093/mnras/stt2374)
- Bolton, J. S., Becker, G. D., Wyithe, J. S. B., Haehnelt, M. G., & Sargent, W. L. W. 2010, *MNRAS*, 406, 612, doi: [10.1111/j.1365-2966.2010.16701.x](https://doi.org/10.1111/j.1365-2966.2010.16701.x)
- Bolton, J. S., Oh, S. P., & Furlanetto, S. R. 2009a, *MNRAS*, 395, 736
- , 2009b, *MNRAS*, 396, 2405
- Bolton, J. S., Viel, M., Kim, T.-S., Haehnelt, M. G., & Carswell, R. F. 2008, *MNRAS*, 386, 1131, doi: [10.1111/j.1365-2966.2008.13114.x](https://doi.org/10.1111/j.1365-2966.2008.13114.x)
- Bolton, J. S., et al. 2012, *MNRAS*, 419, 2880
- Bosman, S. E. I., Fan, X., Jiang, L., et al. 2018, *MNRAS*, doi: [10.1093/mnras/sty1344](https://doi.org/10.1093/mnras/sty1344)
- Bovy, J., Hogg, D. W., & Roweis, S. T. 2011a, *Annals of Applied Statistics*, 5, doi: [10.1214/10-AOAS439](https://doi.org/10.1214/10-AOAS439)

- Bovy, J., Hennawi, J. F., Hogg, D. W., et al. 2011b, *ApJ*, 729, 141, doi: [10.1088/0004-637X/729/2/141](https://doi.org/10.1088/0004-637X/729/2/141)
- Bryan, G. L., & Machacek, M. E. 2000, *ApJ*, 534, 57, doi: [10.1086/308735](https://doi.org/10.1086/308735)
- Calura, F., Tescari, E., D’Odorico, V., et al. 2012, *MNRAS*, 422, 3019
- Cardelli, J. A., Clayton, G. C., & Mathis, J. S. 1989, *ApJ*, 345, 245
- Chambers, K. C., Magnier, E. A., Metcalfe, N., et al. 2016, *ArXiv e-prints*. <https://arxiv.org/abs/1612.05560>
- Chardin, J., Haehnelt, M. G., Aubert, D., & Puchwein, E. 2015, *MNRAS*, 453, 2943, doi: [10.1093/mnras/stv1786](https://doi.org/10.1093/mnras/stv1786)
- Chardin, J., Puchwein, E., & Haehnelt, M. G. 2017, *MNRAS*, 465, 3429, doi: [10.1093/mnras/stw2943](https://doi.org/10.1093/mnras/stw2943)
- Compostella, M., Cantalupo, S., & Porciani, C. 2013, *MNRAS*, 435, 3169, doi: [10.1093/mnras/stt1510](https://doi.org/10.1093/mnras/stt1510)
- . 2014, *MNRAS*, 445, 4186, doi: [10.1093/mnras/stu2035](https://doi.org/10.1093/mnras/stu2035)
- Croft, R. A. C., Weinberg, D. H., Katz, N., & Hernquist, L. 1997, *ApJ*, 488, 532
- D’Aloisio, A., McQuinn, M., Davies, F. B., & Furlanetto, S. R. 2018, *MNRAS*, 473, 560, doi: [10.1093/mnras/stx2341](https://doi.org/10.1093/mnras/stx2341)
- D’Aloisio, A., McQuinn, M., & Trac, H. 2015, *ApJL*, 813, L38, doi: [10.1088/2041-8205/813/2/L38](https://doi.org/10.1088/2041-8205/813/2/L38)
- D’Aloisio, A., Upton Sanderbeck, P. R., McQuinn, M., Trac, H., & Shapiro, P. R. 2017, *MNRAS*, 468, 4691, doi: [10.1093/mnras/stx711](https://doi.org/10.1093/mnras/stx711)
- Davies, F. B., Becker, G. D., & Furlanetto, S. R. 2018a, *ApJ*, 860, 155, doi: [10.3847/1538-4357/aac2d6](https://doi.org/10.3847/1538-4357/aac2d6)
- Davies, F. B., & Furlanetto, S. R. 2014, *MNRAS*, 437, 1141
- Davies, F. B., & Furlanetto, S. R. 2016, *MNRAS*, 460, 1328, doi: [10.1093/mnras/stw931](https://doi.org/10.1093/mnras/stw931)
- Davies, F. B., Furlanetto, S. R., & Dixon, K. L. 2017, *MNRAS*, 465, 2886
- Davies, F. B., Hennawi, J. F., Bañados, E., et al. 2018b, *ApJ*, 864, 142, doi: [10.3847/1538-4357/aad6dc](https://doi.org/10.3847/1538-4357/aad6dc)
- Eilers, A.-C., Davies, F. B., & Hennawi, J. F. 2018, *ApJ*, 864, 53, doi: [10.3847/1538-4357/aad4fd](https://doi.org/10.3847/1538-4357/aad4fd)
- Eilers, A.-C., Davies, F. B., Hennawi, J. F., et al. 2017, *ApJ*, 840, 24, doi: [10.3847/1538-4357/aa6c60](https://doi.org/10.3847/1538-4357/aa6c60)
- Fan, X., et al. 2006, *AJ*, 132, 117
- Fardal, M. A., Giroux, M. L., & Shull, J. M. 1998, *AJ*, 115, 2206
- Faucher-Giguère, C.-A., Lidz, A., Hernquist, L., & Zaldarriaga, M. 2008, *ApJ*, 688, 85
- Faucher-Giguère, C.-A., Lidz, A., Zaldarriaga, M., & Hernquist, L. 2009, *ApJ*, 703, 1416
- Fechner, C., & Reimers, D. 2007, *A&A*, 461, 847
- Fechner, C., et al. 2006, *A&A*, 455, 91
- Feldman, G. J., & Cousins, R. D. 1998, *Phys. Rev. D*, 57, 3873
- Furlanetto, S. R. 2009, *ApJ*, 703, 702
- Furlanetto, S. R., & Dixon, K. 2010, *ApJ*, 714, 355
- Furlanetto, S. R., & Oh, S. P. 2005, *MNRAS*, 363, 1031, doi: [10.1111/j.1365-2966.2005.09505.x](https://doi.org/10.1111/j.1365-2966.2005.09505.x)
- Furlanetto, S. R., & Oh, S. P. 2008a, *ApJ*, 681, 1
- . 2008b, *ApJ*, 682, 14
- Garaldi, E., Compostella, M., & Porciani, C. 2019, *MNRAS*, 483, 5301, doi: [10.1093/mnras/sty3414](https://doi.org/10.1093/mnras/sty3414)
- Garzilli, A., Bolton, J. S., Kim, T.-S., Leach, S., & Viel, M. 2012, *MNRAS*, 424, 1723, doi: [10.1111/j.1365-2966.2012.21223.x](https://doi.org/10.1111/j.1365-2966.2012.21223.x)
- Giallongo, E., Grazian, A., Fiore, F., et al. 2015, *A&A*, 578, A83, doi: [10.1051/0004-6361/201425334](https://doi.org/10.1051/0004-6361/201425334)
- Gleser, L., Nusser, A., Benson, A. J., Ohno, H., & Sugiyama, N. 2005, *MNRAS*, 361, 1399
- Green, J. C., et al. 2012, *ApJ*, 744, 60
- Haardt, F., & Madau, P. 2012, *ApJ*, 746, 125
- Haehnelt, M. G., & Steinmetz, M. 1998, *MNRAS*, 298, L21, doi: [10.1046/j.1365-8711.1998.01879.x](https://doi.org/10.1046/j.1365-8711.1998.01879.x)
- Heap, S. R., et al. 2000, *ApJ*, 534, 69
- Hiss, H., Walther, M., Hennawi, J. F., et al. 2018, *ApJ*, 865, 42, doi: [10.3847/1538-4357/aada86](https://doi.org/10.3847/1538-4357/aada86)
- Hogan, C. J., Anderson, S. F., & Rugers, M. H. 1997, *AJ*, 113, 1495
- Hopkins, P. F., Richards, G. T., & Hernquist, L. 2007, *ApJ*, 654, 731, doi: [10.1086/509629](https://doi.org/10.1086/509629)
- Hui, L., & Gnedin, N. Y. 1997, *MNRAS*, 292, 27
- Inoue, A. K., Shimizu, I., Iwata, I., & Tanaka, M. 2014, *MNRAS*, 442, 1805, doi: [10.1093/mnras/stu936](https://doi.org/10.1093/mnras/stu936)
- Jakobsen, P., et al. 1994, *Nature*, 370, 35
- Jiang, L., McGreer, I. D., Fan, X., et al. 2016, *ApJ*, 833, 222, doi: [10.3847/1538-4357/833/2/222](https://doi.org/10.3847/1538-4357/833/2/222)
- Keating, L. C., Puchwein, E., & Haehnelt, M. G. 2018, *MNRAS*, 477, 5501, doi: [10.1093/mnras/sty968](https://doi.org/10.1093/mnras/sty968)
- Khaire, V. 2017, *MNRAS*, 471, 255, doi: [10.1093/mnras/stx1487](https://doi.org/10.1093/mnras/stx1487)
- Khrykin, I. S., Hennawi, J. F., McQuinn, M., & Worseck, G. 2016, *ApJ*, 824, 133, doi: [10.3847/0004-637X/824/2/133](https://doi.org/10.3847/0004-637X/824/2/133)
- Khrykin, I. S., Hennawi, J. F., & Worseck, G. 2019, *MNRAS*, 484, 3897, doi: [10.1093/mnras/stz135](https://doi.org/10.1093/mnras/stz135)
- Kriss, G. A., et al. 2001, *Sci*, 293, 1112
- Kulkarni, G., Keating, L. C., Haehnelt, M. G., et al. 2018a, *arXiv e-prints*. <https://arxiv.org/abs/1809.06374>
- Kulkarni, G., Worseck, G., & Hennawi, J. F. 2018b, *ArXiv e-prints*. <https://arxiv.org/abs/1807.09774>
- La Plante, P., & Trac, H. 2016, *ApJ*, 828, 90, doi: [10.3847/0004-637X/828/2/90](https://doi.org/10.3847/0004-637X/828/2/90)
- La Plante, P., Trac, H., Croft, R., & Cen, R. 2017, *ApJ*, 841, 87, doi: [10.3847/1538-4357/aa7136](https://doi.org/10.3847/1538-4357/aa7136)
- Lee, K.-G., Hennawi, J. F., Spergel, D. N., et al. 2015, *ApJ*, 799, 196, doi: [10.1088/0004-637X/799/2/196](https://doi.org/10.1088/0004-637X/799/2/196)
- Lidz, A., Faucher-Giguère, C.-A., Dall’Aglio, A., et al. 2010, *ApJ*, 718, 199

- Lukić, Z., Stark, C. W., Nugent, P., et al. 2015, *MNRAS*, 446, 3697, doi: [10.1093/mnras/stu2377](https://doi.org/10.1093/mnras/stu2377)
- Madau, P. 2017, *ApJ*, 851, 50, doi: [10.3847/1538-4357/aa9715](https://doi.org/10.3847/1538-4357/aa9715)
- Madau, P., & Haardt, F. 2015, *ApJL*, 813, L8, doi: [10.1088/2041-8205/813/1/L8](https://doi.org/10.1088/2041-8205/813/1/L8)
- Madau, P., Haardt, F., & Rees, M. J. 1999, *ApJ*, 514, 648
- Madau, P., & Meiksin, A. 1994, *ApJ*, 433, L53
- Martin, D. C., et al. 2005, *ApJ*, 619, L1
- Matsuoka, Y., Strauss, M. A., Kashikawa, N., et al. 2018, *ApJ*, 869, 150, doi: [10.3847/1538-4357/aace7a](https://doi.org/10.3847/1538-4357/aace7a)
- McDonald, P., Miralda-Escudé, J., Rauch, M., et al. 2001, *ApJ*, 562, 52
- McGreer, I. D., Fan, X., Jiang, L., & Cai, Z. 2018, *AJ*, 155, 131, doi: [10.3847/1538-3881/aaaab4](https://doi.org/10.3847/1538-3881/aaaab4)
- McGreer, I. D., Jiang, L., Fan, X., et al. 2013, *ApJ*, 768, 105, doi: [10.1088/0004-637X/768/2/105](https://doi.org/10.1088/0004-637X/768/2/105)
- McQuinn, M. 2009, *ApJ*, 704, L89
- McQuinn, M., & Upton Sanderbeck, P. R. 2016, *MNRAS*, 456, 47, doi: [10.1093/mnras/stv2675](https://doi.org/10.1093/mnras/stv2675)
- McQuinn, M., & Worseck, G. 2014, *MNRAS*, 440, 2406, doi: [10.1093/mnras/stu242](https://doi.org/10.1093/mnras/stu242)
- McQuinn, M., et al. 2009, *ApJ*, 694, 842
- Meiksin, A., & Tittley, E. R. 2012, *MNRAS*, 423, 7, doi: [10.1111/j.1365-2966.2011.20380.x](https://doi.org/10.1111/j.1365-2966.2011.20380.x)
- Miralda-Escudé, J., Haehnelt, M., & Rees, M. J. 2000, *ApJ*, 530, 1
- Mitra, S., Choudhury, T. R., & Ferrara, A. 2018, *MNRAS*, 473, 1416, doi: [10.1093/mnras/stx2443](https://doi.org/10.1093/mnras/stx2443)
- Morrissey, P., et al. 2007, *ApJS*, 173, 682
- Murthy, J. 2014, *ApJS*, 213, 32, doi: [10.1088/0067-0049/213/2/32](https://doi.org/10.1088/0067-0049/213/2/32)
- Oñorbe, J., Hennawi, J. F., & Lukić, Z. 2017, *ApJ*, 837, 106, doi: [10.3847/1538-4357/aa6031](https://doi.org/10.3847/1538-4357/aa6031)
- Parsa, S., Dunlop, J. S., & McLure, R. J. 2018, *MNRAS*, 474, 2904, doi: [10.1093/mnras/stx2887](https://doi.org/10.1093/mnras/stx2887)
- Picard, A., & Jakobsen, P. 1993, *A&A*, 276, 331
- Planck Collaboration, Aghanim, N., Akrami, Y., et al. 2018, *ArXiv e-prints*. <https://arxiv.org/abs/1807.06209>
- Prochaska, J. X., Madau, P., O'Meara, J. M., & Fumagalli, M. 2014, *MNRAS*, 438, 476, doi: [10.1093/mnras/stt2218](https://doi.org/10.1093/mnras/stt2218)
- Proft, S., & Wambsganss, J. 2015, *A&A*, 574, A46, doi: [10.1051/0004-6361/201323280](https://doi.org/10.1051/0004-6361/201323280)
- Puchwein, E., Bolton, J. S., Haehnelt, M. G., et al. 2015, *MNRAS*, 450, 4081, doi: [10.1093/mnras/stv773](https://doi.org/10.1093/mnras/stv773)
- Puchwein, E., Haardt, F., Haehnelt, M. G., & Madau, P. 2019, *MNRAS*, doi: [10.1093/mnras/stz222](https://doi.org/10.1093/mnras/stz222)
- Reimers, D., et al. 1997, *A&A*, 327, 890
- . 2005, *A&A*, 442, 63
- Ricci, F., Marchesi, S., Shankar, F., La Franca, F., & Civano, F. 2017, *MNRAS*, 465, 1915, doi: [10.1093/mnras/stw2909](https://doi.org/10.1093/mnras/stw2909)
- Ricotti, M., Gnedin, N. Y., & Shull, J. M. 2000, *ApJ*, 534, 41
- Rorai, A., Carswell, R. F., Haehnelt, M. G., et al. 2018, *MNRAS*, 474, 2871, doi: [10.1093/mnras/stx2862](https://doi.org/10.1093/mnras/stx2862)
- Rorai, A., Becker, G. D., Haehnelt, M. G., et al. 2017a, *MNRAS*, 466, 2690, doi: [10.1093/mnras/stw2917](https://doi.org/10.1093/mnras/stw2917)
- Rorai, A., Hennawi, J. F., Oñorbe, J., et al. 2017b, *Science*, 356, 418, doi: [10.1126/science.aaf9346](https://doi.org/10.1126/science.aaf9346)
- Rudie, G. C., Steidel, C. C., & Pettini, M. 2012, *ApJL*, 757, L30, doi: [10.1088/2041-8205/757/2/L30](https://doi.org/10.1088/2041-8205/757/2/L30)
- Sahnow, D. J., Penton, S., Ake, T., et al. 2016, in *Proc. SPIE, Vol. 9905, Society of Photo-Optical Instrumentation Engineers (SPIE) Conference Series*, 99052T
- Schaye, J., Theuns, T., Rauch, M., Efstathiou, G., & Sargent, W. L. W. 2000, *MNRAS*, 318, 817
- Schlegel, D. J., Finkbeiner, D. P., & Davis, M. 1998, *ApJ*, 500, 525
- Schmidt, T. M., Hennawi, J. F., Worseck, G., et al. 2018, *ApJ*, 861, 122, doi: [10.3847/1538-4357/aac8e4](https://doi.org/10.3847/1538-4357/aac8e4)
- Shull, J. M., Tumlinson, J., Giroux, M. L., Kriss, G. A., & Reimers, D. 2004, *ApJ*, 600, 570
- Shull, J. M., et al. 2010, *ApJ*, 722, 1312
- Smette, A., Heap, S. R., Williger, G. M., et al. 2002, *ApJ*, 564, 542
- Sokasian, A., Abel, T., & Hernquist, L. 2002, *MNRAS*, 332, 601
- Syphers, D., Anderson, S. F., Zheng, W., et al. 2012, *AJ*, 143, 100
- Syphers, D., & Shull, J. M. 2013, *ApJ*, 765, 119
- Syphers, D., & Shull, J. M. 2014, *ApJ*, 784, 42, doi: [10.1088/0004-637X/784/1/42](https://doi.org/10.1088/0004-637X/784/1/42)
- Syphers, D., et al. 2009a, *ApJ*, 690, 1181
- . 2009b, *ApJS*, 185, 20
- Theuns, T., Leonard, A., Efstathiou, G., Pearce, F. R., & Thomas, P. A. 1998, *MNRAS*, 301, 478, doi: [10.1046/j.1365-8711.1998.02040.x](https://doi.org/10.1046/j.1365-8711.1998.02040.x)
- Theuns, T., Schaye, J., Zaroubi, S., et al. 2002, *ApJL*, 567, L103, doi: [10.1086/339998](https://doi.org/10.1086/339998)
- Theuns, T., Zharoubi, S., Kim, T.-S., Tzanavaris, P., & Carswell, R. F. 2002, *MNRAS*, 332, 367
- Tittley, E. R., & Meiksin, A. 2007, *MNRAS*, 380, 1369
- Viel, M., Bolton, J. S., & Haehnelt, M. G. 2009, *MNRAS*, 399, L39, doi: [10.1111/j.1745-3933.2009.00720.x](https://doi.org/10.1111/j.1745-3933.2009.00720.x)
- Wakker, B. P., Hernandez, A. K., French, D. M., et al. 2015, *ApJ*, 814, 40, doi: [10.1088/0004-637X/814/1/40](https://doi.org/10.1088/0004-637X/814/1/40)
- Walther, M., Hennawi, J. F., Hiss, H., et al. 2018, *ApJ*, 852, 22, doi: [10.3847/1538-4357/aa9c81](https://doi.org/10.3847/1538-4357/aa9c81)
- Walther, M., Oñorbe, J., Hennawi, J. F., & Lukić, Z. 2019, *ApJ*, 872, 13, doi: [10.3847/1538-4357/aafad1](https://doi.org/10.3847/1538-4357/aafad1)
- Wang, F., Yang, J., Fan, X., et al. 2018, *arXiv e-prints*. <https://arxiv.org/abs/1810.11926>
- Worseck, G., & Prochaska, J. X. 2011, *ApJ*, 728, 23
- Worseck, G., Prochaska, J. X., Hennawi, J. F., & McQuinn, M. 2016, *ApJ*, 825, 144, doi: [10.3847/0004-637X/825/2/144](https://doi.org/10.3847/0004-637X/825/2/144)
- Worseck, G., et al. 2011, *ApJ*, 733, L24

- Wright, E. L., Eisenhardt, P. R. M., Mainzer, A. K., et al. 2010, *AJ*, 140, 1868, doi: [10.1088/0004-6256/140/6/1868](https://doi.org/10.1088/0004-6256/140/6/1868)
- Wyithe, J. S. B., & Loeb, A. 2003, *ApJ*, 586, 693
- Zaldarriaga, M., Hui, L., & Tegmark, M. 2001, *ApJ*, 557, 519, doi: [10.1086/321652](https://doi.org/10.1086/321652)
- Zheng, W., Syphers, D., Meiksin, A., et al. 2015, *ApJ*, 806, 142, doi: [10.1088/0004-637X/806/1/142](https://doi.org/10.1088/0004-637X/806/1/142)
- Zheng, W., et al. 2004a, *AJ*, 127, 656
- . 2004b, *ApJ*, 605, 631
- Zheng, W., et al. 2005, in *IAU Colloquium 199: Probing Galaxies through Quasar Absorption Lines*, ed. P. R. Williams, C. Shu, & B. Ménard (Cambridge University Press), 484
- . 2008, *ApJ*, 686, 195

APPENDIX

A. MEASURED HE II EFFECTIVE OPTICAL DEPTHS

Table 7 (continued)

Table 7. Measured τ_{eff} in new or reanalyzed spectra (Table 1)

Quasar	z	τ_{eff}	stat. 1σ error	sys. error	Quasar	z	τ_{eff}	stat. 1σ error	sys. error	
HS 1024+1849	2.60	1.69	+0.61	+0.00	HE2QS J0916+2408	2.80	2.06	+0.08	+0.03	
			-0.01	-0.21				-0.12	-0.00	
	2.64	1.12	+0.10	+0.00		2.84	2.63	2.74	+0.09	+0.00
			-0.03	-0.04					-0.01	-0.04
	2.68	2.19	+0.08	+0.03		2.88	5.02	5.02	+0.07	+0.00
			-0.11	-0.00					-0.07	-0.00
	2.72	2.73	+0.15	+0.00		2.92	4.66	4.66	+0.45	+0.00
			-0.09	-0.03					-0.28	-0.03
	2.76	3.04	+0.18	+0.00		3.08	4.47	4.47	+0.43	+0.01
			-0.09	-0.04					-0.28	-0.03
Q 1602+576	2.56	1.37	+0.24	+0.00	3.12	5.36	5.36	+1.03	+0.38	
			-0.15	-0.04				-0.52	-0.05	
	2.60	1.43	+0.04	+0.05	3.16	3.30	3.30	+0.09	+0.01	
			-0.11	-0.00				-0.10	-0.00	
	2.64	1.09	+0.04	+0.00	3.20	4.07	4.07	+0.22	+0.00	
			-0.03	+0.00				-0.16	-0.03	
	2.68	1.58	+0.03	+0.00	3.24	5.70	5.70	+∞	+0.00	
			-0.03	-0.00				-0.00	-0.00	
	2.72	1.75	+0.02	+0.00	2.80	1.56	1.56	+0.06	+0.00	
			-0.04	-0.00				-0.06	-0.00	
2.76	1.55	+0.02	+0.00	2.84	1.47	1.47	+0.05	+0.00		
		-0.02	-0.00				-0.05	-0.00		
2.80	2.29	+0.02	+0.02	2.88	1.93	1.93	+0.08	+0.00		
		-0.05	-0.00				-0.07	-0.00		
HE2QS J2157+2330	2.68	2.42	+0.18	+0.03	3.12	5.57	5.57	+∞	+0.00	
			-0.19	-0.00				-0.00	-0.00	
	2.72	2.24	+0.13	+0.00	3.16	5.42	5.42	+∞	+0.00	
			-0.12	-0.00				-0.00	-0.00	
	2.76	2.01	+0.09	+0.00	3.20	5.56	5.56	+∞	+0.00	
			-0.09	-0.00				-0.00	-0.00	
	2.80	1.68	+0.07	+0.00	3.36	5.29	5.29	+∞	+0.00	
			-0.07	-0.00				-0.00	-0.00	
	2.84	2.26	+0.09	+0.00	2.84	2.95	2.95	+0.15	+0.01	
			-0.09	-0.00				-0.13	-0.00	
2.88	2.20	+0.10	+0.00	2.88	2.62	2.62	+0.10	+0.01		
		-0.09	-0.00				-0.11	-0.00		
HE2QS J2149-0859	2.72	1.17	+0.16	+0.01	3.12	3.38	3.38	+0.18	+0.01	
			-0.13	-0.01				-0.16	-0.00	
	2.76	1.52	+0.13	+0.02	3.16	3.02	3.02	+0.14	+0.00	
			-0.13	-0.00				-0.13	-0.00	
	2.80	4.19	+∞	+0.00	3.20	5.42	5.42	+∞	+0.00	
			-0.00	-0.00				-0.00	-0.00	
	2.84	1.83	+0.14	+0.02	3.24	5.54	5.54	+∞	+0.00	
			-0.12	-0.01				-0.00	-0.00	
	2.88	1.91	+0.15	+0.02	3.36	5.57	5.57	+∞	+0.00	
			-0.14	-0.00				-0.00	-0.00	
3.12	4.50	+∞	+0.00	2.84	3.13	3.13	+0.14	+0.00		
		-0.00	-0.00				-0.13	-0.00		
3.16	4.39	+∞	+0.00	2.88	2.56	2.56	+0.09	+0.00		
		-0.00	-0.00				-0.08	-0.00		
3.20	4.41	+∞	+0.00	3.12	5.36	5.36	+1.05	+0.36		
		-0.00	-0.00				-0.55	-0.00		
Q 0302-003	2.76	1.75	+0.06	+0.00	3.16	5.74	5.74	+∞	+0.00	
			-0.06	-0.00				-0.00	-0.00	
	2.80	2.17	+0.07	+0.00	3.20	5.76	5.76	+∞	+0.00	
			-0.07	-0.00				-0.00	-0.00	
	2.84	2.07	+0.05	+0.00	3.20	5.60	5.60	+∞	+0.00	
			-0.05	-0.00				-0.00	-0.00	
	2.88	3.74	+0.22	+0.04	3.36	5.88	5.88	+∞	+0.00	
			-0.18	-0.02				-0.00	-0.00	
	2.92	4.34	+0.45	+0.04	3.40	5.94	5.94	+∞	+0.00	
			-0.27	-0.06				-0.00	-0.00	
3.08	5.29	+0.93	+0.60	3.44	5.81	5.81	+∞	+0.00		
		-0.54	-0.04				-0.00	-0.00		
3.12	5.73	+∞	+0.00	HE2QS J2311-1417	3.08	3.25	+0.14	+0.00		
		-0.00	-0.00				-0.13	-0.00		
3.16	4.41	+0.30	+0.07	3.12	3.91	3.91	+0.24	+0.02		
		-0.24	-0.03				-0.21	-0.00		
HE2QS J0233-0149	2.68	2.12	+0.32	+0.00	3.16	5.22	5.22	+1.04	+0.27	
			-0.22	-0.01				-0.56	-0.00	
	2.72	1.93	+0.15	+0.00	3.20	5.60	5.60	+∞	+0.00	
			-0.13	-0.00				-0.00	-0.00	
	2.76	2.32	+0.13	+0.00	3.24	5.56	5.56	+∞	+0.00	
			-0.12	-0.00				-0.00	-0.00	
	2.80	1.84	+0.09	+0.00	3.36	5.40	5.40	+∞	+0.00	
			-0.09	-0.00				-0.00	-0.00	
	2.84	1.47	+0.07	+0.00	3.40	5.39	5.39	+∞	+0.00	
			-0.06	-0.00				-0.00	-0.00	
2.88	3.16	+0.21	+0.02	3.44	5.24	5.24	+∞	+0.00		
		-0.18	-0.00				-0.00	-0.00		
3.08	2.14	+0.08	+0.00	3.48	5.17	5.17	+∞	+0.00		
		-0.09	-0.00				-0.00	-0.00		
3.12	2.89	+0.14	+0.00	3.52	5.12	5.12	+∞	+0.00		
		-0.13	-0.00				-0.00	-0.00		
3.16	5.21	+∞	+0.00	3.56	5.19	5.19	+∞	+0.00		
		-0.00	-0.00				-0.00	-0.00		
3.20	5.37	+∞	+0.00	3.60	5.12	5.12	+∞	+0.00		
		-0.00	-0.00				-0.00	-0.00		
3.24	4.45	+0.64	+0.06	3.64	5.01	5.01	+∞	+0.00		
		-0.40	-0.00				-0.00	-0.00		
HS 0911+4809	2.72	2.12	+0.08	+0.00	SDSS J1137+6237	3.16	5.23	+∞	+0.00	
			-0.07	-0.00				-0.00	-0.00	

Table 7 continued

Table 7 continued

Table 7 (continued)

Quasar	z	τ_{eff}	stat. 1σ error	sys. error
	3.40	5.02	+∞	+0.00
			-0.00	-0.00
	3.52	4.80	+∞	+0.00
			-0.00	-0.00
	3.56	4.80	+∞	+0.00
			-0.00	-0.00
	3.60	4.77	+∞	+0.00
			-0.00	-0.00
	3.64	4.71	+∞	+0.00
			-0.00	-0.00
	3.68	4.68	+∞	+0.00
			-0.00	-0.00
	3.72	3.96	+0.84	+0.40
			-0.46	-0.08
HE2QS J1630+0435	3.08	1.63	+0.06	+0.00
			-0.06	-0.00
	3.12	4.14	+0.36	+0.02
			-0.27	-0.00
	3.16	5.44	+∞	+0.00
			-0.00	-0.00
	3.20	5.51	+∞	+0.00
			-0.00	-0.00
	3.24	5.46	+∞	+0.00
			-0.00	-0.00
	3.36	5.28	+∞	+0.00
			-0.00	-0.00
	3.40	5.39	+∞	+0.00
			-0.00	-0.00
	3.44	5.35	+∞	+0.00
			-0.00	-0.00
	3.48	4.89	+1.05	+0.30
			-0.59	-0.00
	3.52	5.32	+∞	+0.00
			-0.00	-0.00
	3.56	5.37	+∞	+0.00
			-0.00	-0.00
	3.60	3.86	+0.42	+0.00
			-0.31	-0.00
	3.64	5.27	+∞	+0.00
			-0.00	-0.00
	3.68	5.30	+∞	+0.00
			-0.00	-0.00
	3.72	5.29	+∞	+0.00
			-0.00	-0.00
SDSS J1614+4859	3.20	4.86	+∞	+0.00
			-0.00	-0.00
	3.36	4.68	+∞	+0.00
			-0.00	-0.00
	3.40	4.73	+∞	+0.00
			-0.00	-0.00
	3.52	4.56	+∞	+0.00
			-0.00	-0.00
	3.56	4.58	+∞	+0.00
			-0.00	-0.00
	3.60	4.52	+∞	+0.00
			-0.00	-0.00
	3.64	4.47	+∞	+0.00
			-0.00	-0.00
	3.68	4.46	+∞	+0.00
			-0.00	-0.00
	3.72	4.38	+∞	+0.00
			-0.00	-0.00
SDSS J1711+6052	3.36	5.38	+1.16	+1.30
			-0.59	-0.07
	3.40	4.43	+0.40	+0.08
			-0.28	-0.05
	3.52	5.45	+∞	+0.00
			-0.00	-0.00
	3.56	5.45	+∞	+0.00
			-0.00	-0.00
	3.60	5.39	+∞	+0.00
			-0.00	-0.00
	3.64	5.34	+∞	+0.00
			-0.00	-0.00
	3.68	5.29	+∞	+0.00
			-0.00	-0.00
	3.72	5.19	+∞	+0.00
			-0.00	-0.00
	3.76	5.15	+∞	+0.00
			-0.00	-0.00
SDSS J1319+5202	3.20	5.40	+∞	+0.00
			-0.00	-0.00
	3.36	5.06	+∞	+0.00
			-0.00	-0.00
	3.40	4.85	+1.18	+1.32
			-0.65	-0.00
	3.44	2.39	+0.15	+0.00
			-0.11	-0.01
	3.48	3.97	+0.76	+0.00
			-0.40	-0.02
	3.52	4.72	+∞	+0.00
			-0.00	-0.00
	3.56	4.65	+∞	+0.00
			-0.00	-0.00
	3.60	4.53	+∞	+0.00
			-0.00	-0.00
	3.64	4.46	+∞	+0.00
			-0.00	-0.00
	3.68	3.98	+1.00	+0.34
			-0.54	-0.00
	3.72	4.28	+∞	+0.00
			-0.00	-0.00
	3.76	3.04	+0.44	+0.04
			-0.34	-0.00

Table 7 continued

Table 7 (continued)

Quasar	z	τ_{eff}	stat. 1σ error	sys. error
	3.80	3.59	+1.00	+0.23
			-0.54	-0.00
	3.84	3.38	+0.84	+0.08
			-0.47	-0.00

NOTE—Sensitivity lower limits on τ_{eff} are marked with infinite upper error.

B. CONVERGENCE OF THE HE II EFFECTIVE OPTICAL DEPTHS IN THE NYX SIMULATION

Here we assess the convergence of the He II Ly α forest transmission in our hydrodynamical simulation. Similar to the $z \gtrsim 5$ H I Ly α forest (Bolton & Becker 2009), the high optical depth of the He II Ly α forest at $z > 3$ is difficult to fully resolve in simulations (Compostella et al. 2013, 2014).

Our convergence test simulations consist of a suite of $(20h^{-1} \text{ cMpc})^3$ volumes at $z = 3$ from Lukić et al. (2015) on a series of grids: 256^3 , 512^3 , 1024^3 , and 2048^3 . The fiducial simulation used in this work is most similar to the 1024^3 simulation. In Figure 13 we show the He II Ly α effective optical depth at a fixed $\Gamma_{\text{HeII}} = 10^{-15} \text{ s}^{-1}$ as a function of the spatial resolution in the simulation, with the resolution of our fiducial simulation shown by the vertical dashed line. Similar to the case of H I Ly α , we see a smooth trend of convergence towards higher resolution. We find that a linear fit to τ_{eff} as a function of spatial resolution, shown by the dotted line in Figure 13, very closely matches the trend. Extrapolating this curve to infinite resolution (similar to Lukić et al. 2015, although our functional form differs), we find that our fiducial simulation is unconverged at the $\sim 5\%$ level in τ_{eff} . Based on the relationship between τ_{eff} and Γ_{HeII} , this implies that our Γ_{HeII} measurements may be biased high by $\sim 10\%$.

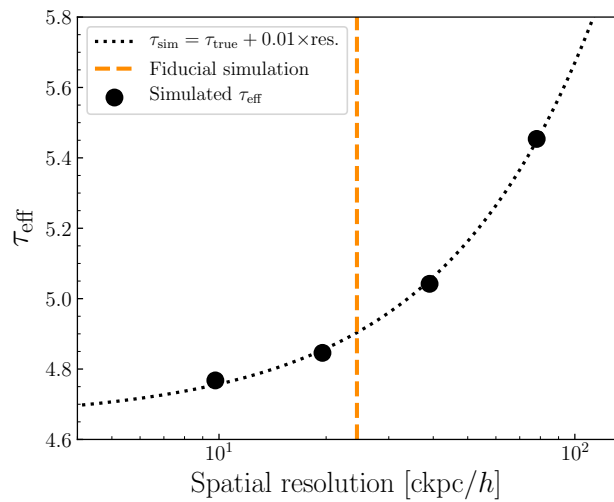


Figure 13. He II effective optical depth as a function of the spatial resolution of four $(20h^{-1} \text{ cMpc})^3$ volumes at $z = 3$, assuming $\Gamma_{\text{HeII}} = 10^{-15} \text{ s}^{-1}$. The dotted line shows a linear fit, while the dashed line indicates the spatial resolution of our fiducial simulation.